



An aquatic-vision-inspired camera based on a monocentric lens and a silicon nanorod photodiode array

Min Sung Kim^{1,2,7}, Gil Ju Lee^{3,7}, Changsoon Choi^{1,2,7}, Min Seok Kim^{3,7}, Mincheol Lee^{1,2}, Siyi Liu⁴, Kyoung Won Cho^{1,2}, Hyun Myung Kim³, Hyojin Cho^{1,2}, Moon Kee Choi⁵, Nanshu Lu⁴, Young Min Song³✉ and Dae-Hyeong Kim^{1,2,6}✉

Conventional wide-field-of-view cameras consist of multi-lens optics and flat image sensor arrays, which makes them bulky and heavy. As a result, they are poorly suited to advanced mobile applications such as drones and autonomous vehicles. In nature, the eyes of aquatic animals consist of a single spherical lens and a highly sensitive hemispherical retina, an approach that could be beneficial in the development of synthetic wide-field-of-view imaging systems. Here, we report an aquatic-vision-inspired camera that consists of a single monocentric lens and a hemispherical silicon nanorod photodiode array. The imaging system features a wide field of view, miniaturized design, low optical aberration, deep depth of field and simple visual accommodation. Furthermore, under vignetting, the photodiode array enables high-quality panoramic imaging due to the enhanced photodetection properties of the silicon nanorod photodiodes.

Miniaturized, lightweight cameras that offer a wide field of view (FoV) are of use in applications that require object tracking capabilities, such as drones and autonomous vehicles^{1,2}. However, due to the large Petzval field curvature in wide FoV imaging, a large number of lenses are required to focus panoramic scenes onto a flat image sensor array^{3,4}. For example, a typical wide-angle camera module, which has a FoV of over 120°, requires between 8 and 13 lenses⁵. This dramatically increases the overall volume and weight of the camera module³ (Supplementary Fig. 1).

Biological imaging systems have been optimized through evolution and have inspired the development of biomimetic cameras^{6–8}. Curved image sensor arrays that mimic the human eye using single plano-convex lenses have, for example, enabled imaging with fewer optical aberrations (Supplementary Fig. 2a)^{9–11}. However, these human-eye-inspired cameras offer limited FoVs of less than 100° due to off-axis aberrations, particularly at large angles (Supplementary Fig. 2b)³. In addition, the natural human eye does not use single-lens optics as it cannot reduce optical aberrations without its cornea, which serves as an additional refractive lens (Supplementary Fig. 2c)¹². Alternatively, compound eye-type imaging systems inspired by arthropod eyes have demonstrated wide-FoV characteristics (Supplementary Fig. 3a)^{13–16}. However, the visual acuity (clarity of vision) of compound eyes is inferior to that of camera-type eyes, such as vertebrate and aquatic animal eyes, because their corneal microlens cannot be miniaturized to have a sufficient diffraction limit (Supplementary Fig. 3b).

Aquatic-type vision, found in fish¹⁷, cephalopods¹⁸ and aquatic mammals¹⁹, features a wide FoV of up to 160°, high visual

acuity, minimal optical aberrations¹⁸, deep depth of field (DoF)²⁰ and simple visual accommodation²¹, all in small form factors⁵. Furthermore, photoreceptors on the retinas of aquatic eyes are highly light-sensitive, which allows high visual acuity even in dim underwater conditions²². Many of these characteristics are a consequence of a single spherical monocentric lens with a parabolic refractive index (RI) profile^{5,17} and a hemispherical curved retina with highly light-sensitive rod cells²³. These features have inspired the development of wide-FoV cameras that meet key requirements for advanced mobile electronics^{24,25}.

In this Article, we report a bio-inspired camera that adopts the unique optical advantages of aquatic vision by integrating a monocentric lens and a hemispherical silicon nanorod photodiode array (h-SiNR-PDA). The nanorod photodiode array has a textured and passivated structure that enhances its light sensitivity, providing improved imaging under vignetting. The aquatic-vision-inspired camera features a FoV of 120°, an 11.5-mm form factor, a DoF of 20 cm to infinity and minimal optical aberrations with simple accommodation.

Structural and functional features of aquatic vision in nature

Figure 1a presents a photograph of an aquatic animal (Cichlid), while the inset shows a corresponding schematic illustration demonstrating the anatomy of its eye. Aquatic vision features a wide FoV with clear visual acuity, even in a dim underwater environment, as a result of the single spherical monocentric lens and highly light-sensitive hemispherical retina^{5,22}. The deep DoF and

¹Center for Nanoparticle Research, Institute for Basic Science (IBS), Seoul, Republic of Korea. ²School of Chemical and Biological Engineering, Institute of Chemical Processes, Seoul National University, Seoul, Republic of Korea. ³School of Electrical Engineering and Computer Science, Gwangju Institute of Science and Technology, Gwangju, Republic of Korea. ⁴Center for Mechanics of Solids, Structures and Materials, Department of Aerospace Engineering and Engineering Mechanics, Department of Biomedical Engineering, Texas Materials Institute, University of Texas at Austin, Austin, TX, USA. ⁵School of Materials Science and Engineering, Ulsan National Institute of Science and Technology (UNIST), Ulsan, Republic of Korea. ⁶Department of Materials Science and Engineering, Seoul National University, Seoul, Republic of Korea. ⁷These authors contributed equally: Min Sung Kim, Gil Ju Lee, Changsoon Choi, Min Seok Kim. ✉e-mail: ymsong@gist.ac.kr; dkim98@snu.ac.kr

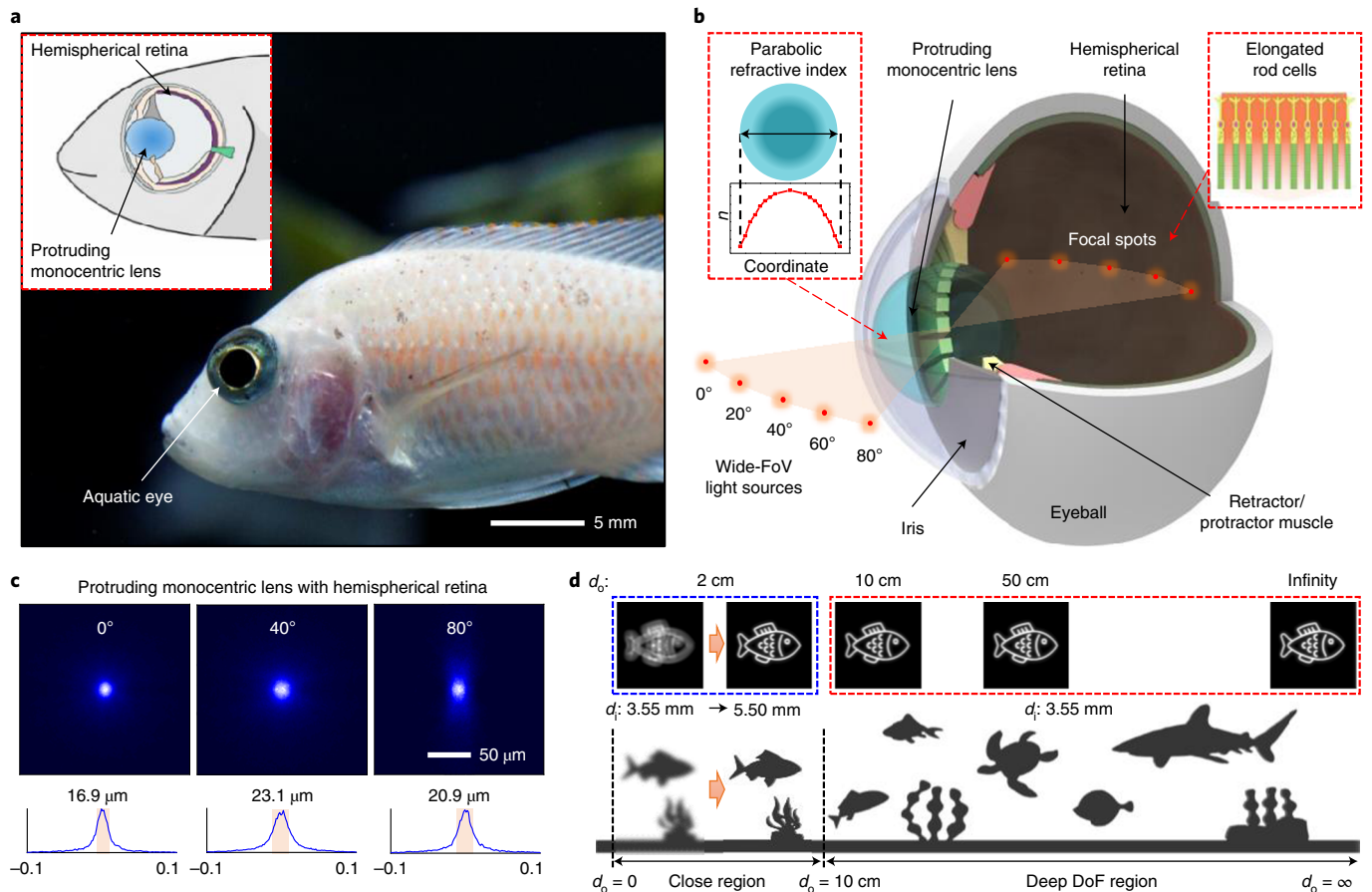


Fig. 1 | Structural and functional features of aquatic vision in nature. **a**, Photograph of an example Cichlid. Inset: an anatomical illustration of the aquatic eye. **b**, Schematic of the aquatic eye with its key features. Left inset: parabolic RI profile of the protruding monocentric lens. Right inset: highly sensitive elongated rod cells in the hemispherical retina. **c**, Optical simulation of light spots focused by the protruding monocentric lens (top) for light sources at three different angles (0°, 40° and 80°). The line graphs (bottom) show corresponding cross-sectional intensity profiles. **d**, The top frames show an optical simulation for focusing objects located at different d_o (for example, 2 cm in the blue dashed box; 10 cm, 50 cm and infinity in the red dashed box). The blurry image for the object located at $d_o = 2$ cm can be refocused by visual accommodation (that is, d_i change from 3.55 mm to 5.50 mm). The bottom frame shows a schematic drawing of the deep DoF.

facile visual accommodation are other unique advantages of aquatic vision²⁰. In nature, such features protect aquatic animals from enemies and help in hunting prey. In the real world, if a similar imaging system were available, such features would be useful for obstacle avoidance and object tracking, particularly in advanced mobile electronics¹.

These optical properties arise from the unique structural and functional features of the aquatic eye: that is, a protruding monocentric lens, a hemispherical retina, an iris and retractor/protractor muscles (Fig. 1b). The protruding monocentric lens, with its spherical and symmetric shape, forms a hemispherical focal plane. By matching this focal plane with the hemispherical retina, aquatic vision achieves a wide FoV. In addition, the parabolic RI profile of the monocentric lens (Fig. 1b, left inset) minimizes optical aberrations, allowing nearly zero aberrations for panoramic scenes. The iris blocks stray light and minimizes optical aberrations further. Meanwhile, the retina contains elongated rod cells (Fig. 1b, right inset) that elongate the light path for better light absorption, and is thus suited to detecting low-intensity light in the dim undersea environment²². The retractor/protractor muscles move the monocentric lens back and forth for visual accommodation.

These characteristics (the wide FoV without optical aberrations, for example) can be confirmed theoretically by means of opti-

cal simulations. A three-dimensional (3D) ray-tracing simulation based on the Monte-Carlo method was used to validate the inherent superiority of the monocentric lens in wide-FoV imaging (Fig. 1c). The aquatic vision can focus light from wide angular directions (<160°) to within a tiny spot on the hemispherical retina, confirming the small coma aberration. The 2D ray-tracing simulation also supports the effective correction of off/on-axis aberrations by the monocentric lens (Supplementary Fig. 4). More details about the ray-tracing simulation are provided in Supplementary Note 1.

Aquatic vision also features a deep DoF resulting from its inherently short focal length, which enables well-focused imaging for objects located at a wide range of distances (Fig. 1d, bottom). A clear image is obtained when the image distance (d_i) is equal to the focal length (d_f) of the monocentric lens for an object located at the object distance (d_o) (Supplementary Fig. 5). In aquatic vision, all objects located at 10 cm or further are clearly imaged by the monocentric lens with $d_i = 3.55$ mm (red dashed box, Fig. 1d; deep DoF region). For closer objects (for example, located at 2 cm), the focal length becomes longer and the image captured with $d_i = 3.55$ mm becomes blurry. However, by slightly modulating d_i to be 5.50 mm using retractor/protractor muscles (Fig. 1b), the blurred image can be easily refocused (blue dashed box, Fig. 1d; close region). Visual accommodation in the aquatic eye is simpler than in the human

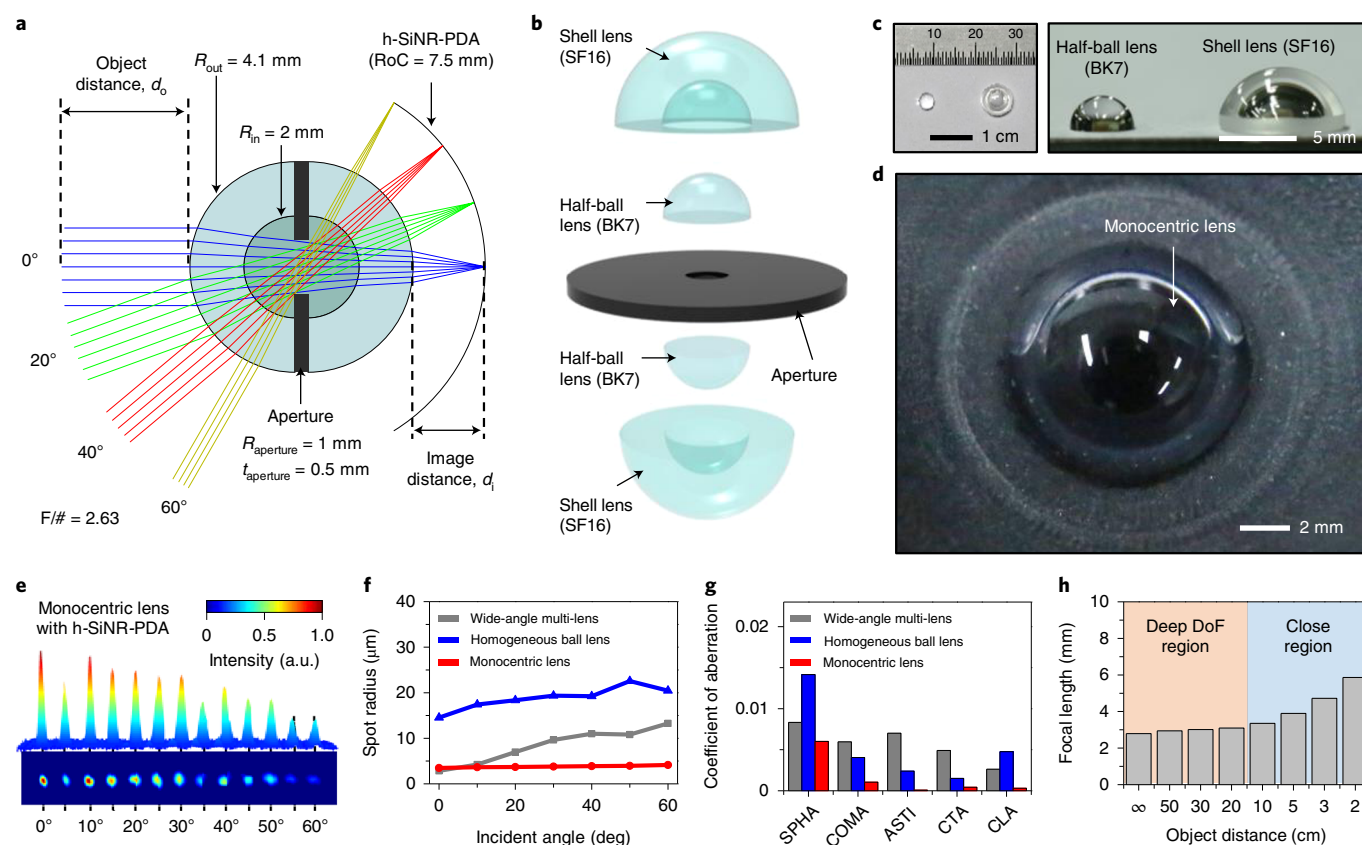


Fig. 2 | Monocentric lens inspired by the protruding monocentric lens of aquatic eyes. **a**, Ray-tracing simulation of the aquatic-vision-inspired camera. RoC, radius of curvature. **b**, Exploded schematic of the monocentric lens. **c**, Photographs showing a disassembled form of the monocentric lens. Top (left) and side (right) views of the inner half-ball lens (BK7) and the outer shell lens (SF16). **d**, Photograph showing an assembled form of the monocentric lens. **e**, Light intensity (top) and size (bottom) of laser spots for different incident angles, focused and detected by using the monocentric lens and h-SiNR-PDA, respectively. **f**, Optical simulation of the monochromatic spot radius for different incident angles. **g**, Seidel aberration coefficients of the monocentric lens and control lenses. **h**, Focal lengths for objects at various distances, focused by the monocentric lens (deep DoF region, red; close region, blue).

eye in terms of optics, because it does not need any changes in the original lens shape (Supplementary Fig. 6a)²¹ (visual accommodation in the human eye requires deformation of the lens; Supplementary Fig. 6b)³.

Monocentric lens inspired by a natural protruding monocentric lens

An artificial imaging system inspired by the natural aquatic eye can be developed by integration of the monocentric lens and h-SiNR-PDA (Fig. 2a). The monocentric lens inspired by the protruding monocentric lens in the aquatic eye (Fig. 1) has a spherical and symmetric shape (Supplementary Fig. 7), where the half-ball lens (BK7) and shell lens (SF16) are assembled on both sides of the aperture using a transparent optical adhesive (NOA 61) (Fig. 2b). Such a symmetric hemispherical lens shape is helpful for eliminating undesired wavefront error. Photographs of the lenses and their assembled form are shown in Fig. 2c,d, respectively. Details of the fabrication process of the monocentric lens are provided in Supplementary Fig. 8 and the Methods.

Such a core-shell structure with two RI values in the monocentric lens (Fig. 2b) is inspired by the parabolic RI profile in the protruding monocentric lens of an aquatic eye (Fig. 1b, left inset). However, in the monocentric lens, the outer shell (SF16, $R_{\text{out}} = 4.1$ mm) is designed to have a larger RI ($n_{\text{out}} = 1.65$) than the inner core (BK7, $R_{\text{in}} = 2$ mm; $n_{\text{in}} = 1.52$) to achieve the small focal spot radius, because the imaging system is under air, not under water

(Supplementary Fig. 9). The optimal RI difference of the lenses ($\Delta n = n_{\text{out}} - n_{\text{in}}$) and the radius ratio ($R_{\text{in}}/R_{\text{out}}$) are around 0.13 and 0.48, respectively (Supplementary Fig. 10). The aperture is placed at the centre of individual half-ball lenses to achieve the wide FoV without intensity attenuation of focused lights (Supplementary Fig. 11). With these optimizations, the monocentric lens with two RI values shows comparable (or better in some conditions) focusing capabilities than the natural protruding monocentric lens or the monocentric lens with three RI values (Supplementary Fig. 12). It also has advantages in terms of fabrication and cost compared to the recently developed lenses (for example, a lens with continuous RI²⁶ and a flat metalens²⁷). More details about the design optimization of the monocentric lens are included in Supplementary Note 2.

The monocentric lens, when integrated with the h-SiNR-PDA inspired by the hemispherical retina of aquatic eyes (Fig. 1b), enables wide-FoV imaging. Because the curved shape of the h-SiNR-PDA is matched with the hemispherical focal plane (Fig. 2a), the monocentric lens effectively focuses the light from wide angular directions without off-axis aberrations, although vignetting (that is, light intensity attenuation at wide angles) is observed (Fig. 2e). On the other hand, significant blurring occurs, particularly at large angles, when a flat photodetector array (f-PDA) is used (Supplementary Fig. 13). In particular, the monochromatic spot radii of the monocentric lens are less than $4.2 \mu\text{m}$ for all incident angles (Fig. 2f and Supplementary Fig. 14); these are much smaller spot radii than

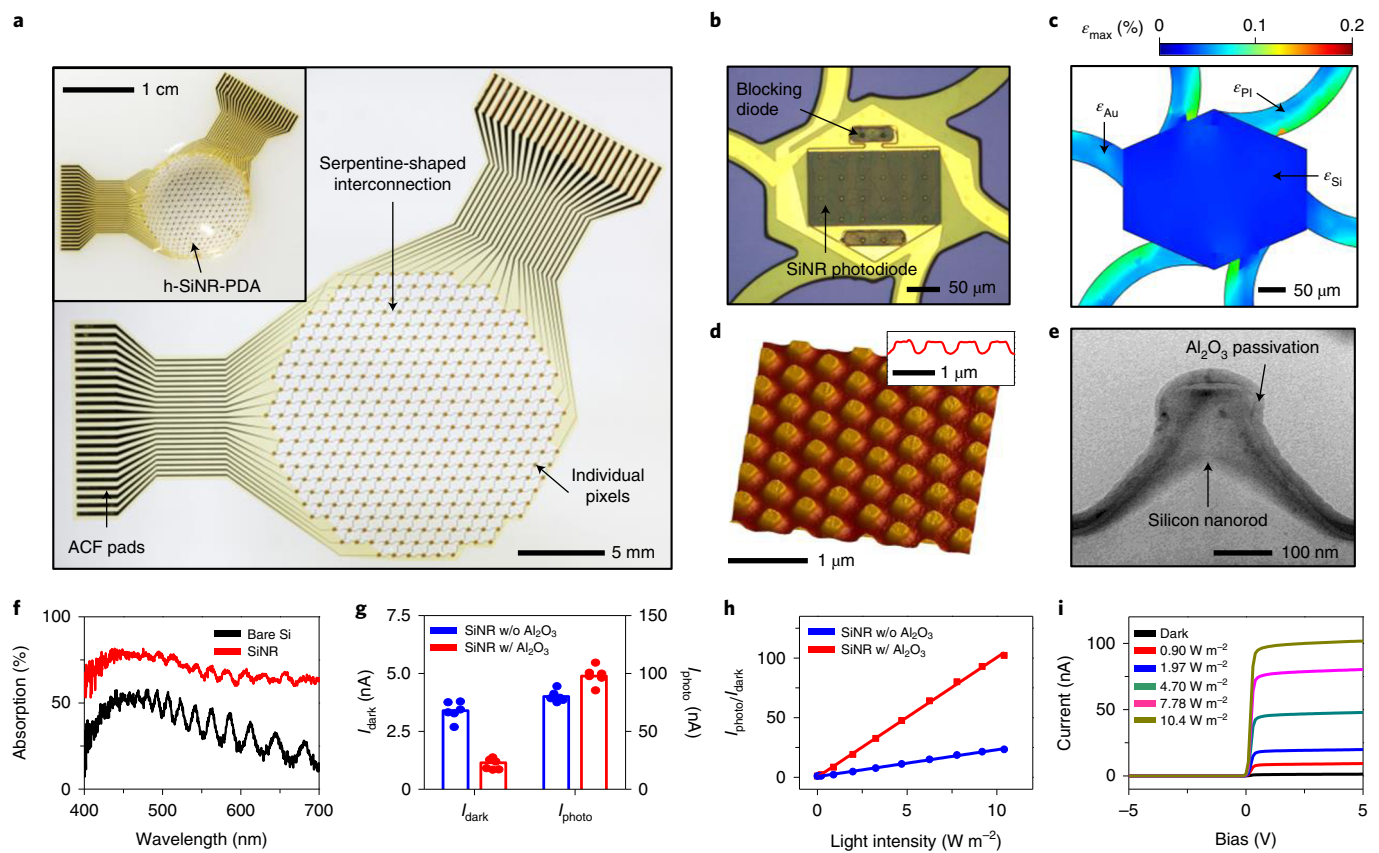


Fig. 3 | h-SiNR-PDA inspired by the retina of aquatic eyes. **a**, Photograph of the SiNR photodiode array fabricated on a flat substrate. ACF, anisotropic conductive film. Inset: photograph of the same array transferred to the hemispherical surface. **b**, Optical microscope image of an individual pixel composed of a photodiode and a blocking diode. **c**, FEA of the strain distribution in the individual pixel of the h-SiNR-PDA. **d**, Three-dimensional (3D) AFM image showing the surface morphology of the SiNRs. Inset: height profile of the SiNRs. **e**, Cross-sectional TEM image of the SiNRs. **f**, Photo-absorption profile of the bare silicon and SiNRs in the visible spectrum range. **g**, Statistical analysis ($N=6$) of I_{dark} and I_{photo} for the SiNR photodiode with and without Al₂O₃ passivation. **h**, Sensitivity ($I_{\text{photo}}/I_{\text{dark}}$) of the SiNR photodiode with and without Al₂O₃ passivation under illumination with various light intensities. **i**, I - V curves of the SiNR photodiode serially connected with the blocking diode under various light intensities.

those of a conventional wide-angle multi-lens or a homogeneous ball lens (Fig. 2f). Furthermore, the achromatic on/off-axis aberrations (for example, spherical aberration (SPHA), coma aberration (COMA), and astigmatism aberration (ASTI)) and chromatic aberrations (for example, chromatic transverse aberration (CTA) and chromatic longitudinal aberration (CLA)) of the monocentric lens are much smaller than those of the wide-angle multi-lens or homogeneous ball lens (Fig. 2g)²⁸. More details about the optical aberration of the monocentric lens compared to control lenses are provided in Supplementary Note 3.

The monocentric lens also has a short d_f ranging between 2.79 mm and 5.87 mm, which enables deep DoF imaging. Figure 2h presents the d_f of the monocentric lens for objects located at various distances. The objects at more than 20 cm (20 cm to infinity) have almost similar d_f values around 2.95 mm (deep DoF region in Fig. 2h). Thus, those objects can be focused well by maintaining $d_{\text{far}}=2.95$ mm (Supplementary Fig. 15a). When objects are closer ($d_o < 20$ cm), d_f gradually changes (close region in Fig. 2h) and the images become blurry (Supplementary Fig. 15b). However, accommodation can be applied easily in the aquatic eye using the retractor and protractor muscles (Fig. 1b). Such blurred images are easily refocused by slightly modulating d_i (Supplementary Fig. 15c,d). This is clearly simpler than the accommodation method of the conventional wide-angle multi-lens system, in which each distance between individual lenses has to be adjusted³.

h-SiNR-PDA inspired by the retina of aquatic eyes

Inspired by the hemispherical retina with elongated rod cells in aquatic eyes (Fig. 1b and right inset), we developed the h-SiNR-PDA, a mesh-shaped 23 × 23-hexagonal-pixel array (Fig. 3a and inset). Individual devices, that is, the nanorod-textured silicon photodiode and blocking diode¹³, are placed inside the hexagonal pixel (Fig. 3b), and connected as a lateral n-p-n configuration for passive matrix array operation (Supplementary Fig. 16)²⁹. The detailed fabrication process for the h-SiNR-PDA is described in Supplementary Fig. 17 and the Methods, and cross-sectional schematic illustrations for the fabrication of an individual pixel are shown in Supplementary Fig. 18.

The mesh array design with serpentine interconnections minimizes induced strain on the array^{30–32}. According to finite element analysis (FEA), induced strain on an individual photodiode is 0.02%, which is much lower than the fracture strain of silicon (~1%)³³ (Fig. 3c). The ultrathin thickness of the array (~5.5 μm), including the thin flexible silicon photodetecting layer (~1.25 μm), is helpful in enhancing the mechanical flexibility of the array^{34,35}. The h-SiNR-PDA could thus be conformally laminated on a concavely hemispherical surface without mechanical fractures (Supplementary Fig. 19a). The pixel distribution at the perimeter of the h-SiNR-PDA is close to a circle, so the array can cover almost the entire hemispherical surface (Supplementary Fig. 19b). More details about the mechanical analysis are provided in Supplementary Note 4.

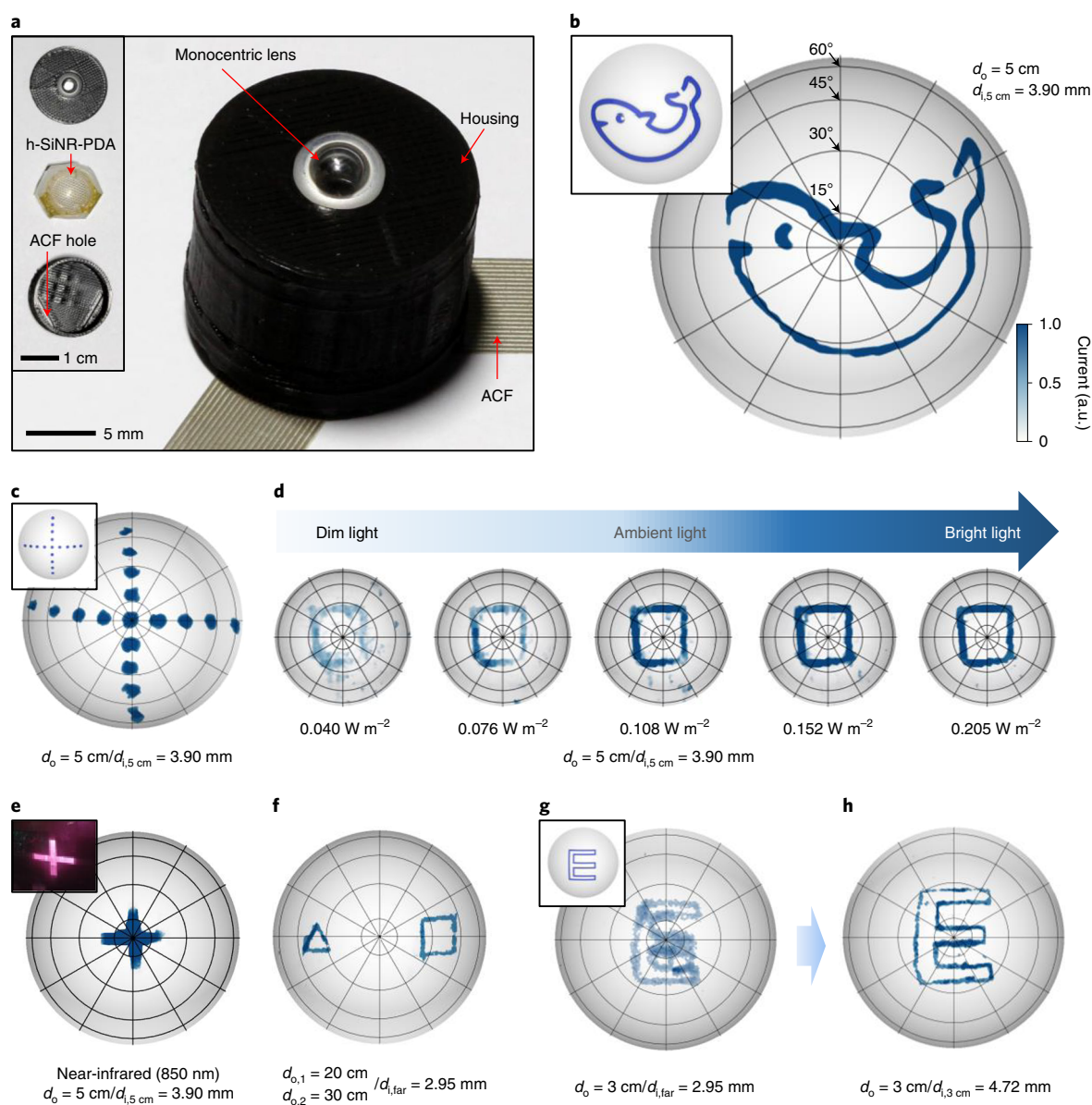


Fig. 4 | Imaging demonstration with the integrated camera module. **a**, Photograph of the assembled aquatic-vision-inspired camera module. Inset: its disassembled form. **b**, Panoramic imaging demonstration (FoV = 120°). Inset: the original object image. **c**, Wide-FoV imaging of a cross pattern composed of spots. The spots are located at various angles (−60° to ~60°). Inset: image of the original spotted cross pattern. **d**, Imaging demonstrations under different focused light intensities from 0.040 W m^{−2} to 0.205 W m^{−2}. **e**, NIR imaging demonstration ($\lambda = 850$ nm). Inset: the original NIR object image. **f**, Imaging demonstration for a triangle (object 1) and square (object 2) located at different distances ($d_{o,1} = 20$ cm and $d_{o,2} = 30$ cm) and at different angles with 90° difference. The image is captured with $d_{i,far} = 2.95$ mm. **g,h**, Imaging demonstration for a close object ($d_o = 3$ cm). The image captured with $d_{i,far} = 2.95$ mm is blurry (**g**), but it can be refocused with $d_{i,3cm} = 4.72$ mm (**h**). Inset: image of the original object.

In wide-FoV imaging, vignetting is a major issue in acquiring clear images. For example, light intensity after passing through a conventional wide-angle multi-lens is drastically attenuated in proportion to the fourth power of the cosine function of the incident angle³⁶. Although the monocentric lens substantially corrects vignetting due to its spherical shape, the intensity of the passed light is still attenuated in proportion to the cosine function of the incident angle³⁶. In addition, the thin flexible silicon photodiodes are accompanied by limited photo-absorption^{37–39}. Accordingly, nanorod texturing and surface passivation are also applied to enhance the photo-absorption and light sensitivity of the photodiode.

Texturing is provided by a silicon nanorod array (Fig. 3d; see inset for an atomic force microscope (AFM) image and height

profile), while a thin Al₂O₃ layer (~25 nm) is used to passivate the textured surface. Figure 3e presents a transmission electron microscope (TEM) image of the nanorods and passivation. The silicon nanorods (SiNRs) have a height of 220 nm, diameter of 200 nm and pitch of 520 nm. The parameters of the SiNRs were engineered according to a wave optics simulation (Supplementary Fig. 20). A large-scale TEM image showing the multiple SiNRs and energy-dispersive spectrometry (EDS) elemental distribution analyses showing the Al₂O₃ layer are provided in Supplementary Fig. 21.

The SiNRs show enhanced photo-absorption in visible spectra compared to bare silicon (Fig. 3f), because the nanorod-textured surface reduces surface reflection and transmission (Supplementary Fig. 22)^{37,40}. Theoretical optical analyses show that the enhanced

photo-absorption of the SiNRs is due to a light trapping effect arising from diffraction at the nanorod structure (Supplementary Figs. 23 and 24). The incident light is diffracted by the nanorod-textured surface and trapped inside the SiNRs due to multiple total internal reflections. Thus, the overall light path for the photo-absorption is elongated⁴⁰. More details of the theoretical optical analyses are provided in Supplementary Note 5.

The nanorod texturing of the silicon surface forms surface dangling bonds that generate a surface leakage current and thereby increase the dark current (I_{dark})⁴¹. Such surface dangling bonds also generate charge carrier recombination sites, which reduce the photocurrent (I_{photo})⁴⁰. To combat this, surface passivation techniques have been used³⁹. Here, Al_2O_3 passivation of the nanorod-textured silicon surface was applied; this suppresses the surface leakage current⁴¹ and inhibits charge carrier recombination⁴⁰ by removing the dangling bonds and thus reduces I_{dark} and enhances I_{photo} (Fig. 3g). With these attributes, the SiNR photodiode with Al_2O_3 passivation can measure incident light with enhanced sensitivity (Fig. 3h). Figure 3i presents I - V curves of the SiNR photodiode with the Al_2O_3 passivation serially connected with the blocking diode under illumination of various light intensities, confirming the sensitive photoresponse of the SiNR photodiode as well as suppression of the reverse bias current by the blocking diode¹³. The dynamic range and photoresponsivity of the SiNR photodiode are as high as 61.2 dB and 0.34 A W^{-1} , respectively (Supplementary Fig. 25). In addition, the photoresponse speed of the SiNR photodiode is comparable to that of a bare silicon photodiode (Supplementary Fig. 26), and it can be improved further by exploiting a shorter intrinsic region length to reduce the transit time as well as by minimizing the parasitic resistance and capacitance^{42,43}.

Imaging demonstrations using the integrated camera module

Integration of the monocentric lens and the h-SiNR-PDA with a custom-made housing results in an aquatic-vision-inspired camera module. The camera module, its components and an exploded schematic illustration are presented in Fig. 4a, its inset and Supplementary Fig. 27, respectively. The aquatic-vision-inspired camera enables aberration-free wide-FoV imaging, but its module size (that is, optical axis length) is only 11.5 mm, which is comparable to the size of a quarter coin (Supplementary Fig. 28). Detailed specifications of the developed camera and those of commercial cameras and other bio-inspired imaging systems are summarized in Supplementary Table 6.

The aquatic-vision-inspired camera enables high-quality aberration-free imaging with wide FoV, deep DoF and facile accommodation, as shown in the optical analyses in Fig. 2. We validated these features with imaging demonstrations for objects located at wide angles and different distances. In the experimental set-up for the imaging demonstration, the position of the monocentric lens was fixed, while the positions of the h-SiNR-PDA and an object (patterned light passing through a shadow mask mounted on a light source) were adjusted using underlying rails. In this way, d_i and d_o could be controlled (Supplementary Fig. 29). The h-SiNR-PDA was connected to the external electronics via an anisotropic conductive film (ACF) and the photocurrent was measured using a customized data acquisition system (Supplementary Fig. 30). More details about the experimental set-up for the imaging demonstration and the data acquisition system with software algorithms are provided in Supplementary Note 6.

The aquatic-vision-inspired camera successfully performs various kinds of wide-FoV imaging without optical aberrations. Figure 4b shows a fish-shaped image captured by the aquatic-vision-inspired camera. The original object image is shown in the inset of Fig. 4b. The captured image is rendered on the hemispherical surface, whose radius matches the curvature of the h-SiNR-PDA. For quantitative

validation of the aberration-free wide-FoV imaging, a cross pattern of spots located at various angles ranging between -60° and 60° , in 15° intervals (Fig. 4c, inset), was imaged by the h-SiNR-PDA. Each spot was imaged without distortion (Fig. 4c). The spots located on the outer side of the cross pattern could also be imaged well by using the pixels at the perimeter of the h-SiNR-PDA (corresponding to wide-FoV imaging). The FoV of the aquatic-vision-inspired camera could be improved up to 160° by using advanced lens manufacturing methods and by employing an image sensor array with a more hemispherical shape (Supplementary Fig. 31).

Because the spherical monocentric lens reduces vignetting and the h-SiNR-PDA exhibits enhanced sensitivity, the aquatic-vision-inspired camera allows us to capture images in a dim environment. Figure 4d shows square patterns captured under different light intensities. The dim square pattern with an intensity of only 0.040 W m^{-2} is imaged well. In addition, the aquatic-vision-inspired camera can perform imaging in the near-infrared (NIR), as the SiNR can absorb NIR light ($\lambda = 850 \text{ nm}$; Fig. 4e). A photograph of the original NIR object is shown in the inset of Fig. 4e.

The aquatic-vision-inspired camera also features a deep DoF due to its inherently short d_f . All objects located at 20 cm or more can be imaged with a single $d_{i,\text{far}} = 2.95 \text{ mm}$ (Supplementary Fig. 32). In another case, two objects (a triangle (object 1) and a square (object 2)) placed at different distances ($d_{o,1} = 20 \text{ cm}$ and $d_{o,2} = 30 \text{ cm}$) and at different angles with 90° difference (Supplementary Fig. 33) can be simultaneously imaged with a single $d_{i,\text{far}} = 2.95 \text{ mm}$ (Fig. 4f). However, if an object located at a close position (for example, $d_o = 3 \text{ cm}$, Fig. 4g, inset) is to be imaged with $d_{i,\text{far}}$, the captured image becomes blurry due to the increased d_f for $d_o = 3 \text{ cm}$ (Fig. 4g). In this case, visual accommodation is needed. The position of the h-SiNR-PDA is adjusted to change d_i to match the increased $d_{f,3\text{cm}} = 4.72 \text{ mm}$. The blurry image of the letter 'E' captured with $d_{i,\text{far}} = 2.95 \text{ mm}$ (Fig. 4g) can then be refocused with an adjusted $d_{i,3\text{cm}} = 4.72 \text{ mm}$ (Fig. 4h).

Conclusions

Inspired by natural aquatic-vision systems, we have developed a miniaturized wide-FoV camera by integrating a monocentric lens with an h-SiNR-PDA. Our camera features a wide FoV, miniaturized design, minimum optical aberration, deep DoF, simple visual accommodation and enhanced light sensitivity. The entire system is enclosed in a single small-form-factor unit, and is fabricated using accessible laboratory-based methods. The aquatic-vision-inspired camera could be of use in a number of emerging technological applications, particularly where obstacle avoidance and object tracking at wide angles is required, and could help expand the current capabilities of advanced mobile electronic devices.

Methods

Fabrication of the monocentric lens and its detailed specifications. To fabricate the monocentric lens, two kinds of lens (BK7 and SF16) were used. The RI (at a wavelength of 588 nm) and RoC of BK7 are 1.52 and 2 mm and those of SF16 are 1.65 and 4.1 mm, respectively. A transparent optical adhesive (NOA 61, Norland Products) with RI of 1.56 was used to fill the space between the lenses. The surface profile of each lens was analysed using a large-area aspheric 3D profiler (UA3P, Panasonic).

Fabrication of the monocentric lens (Supplementary Fig. 8) began with drop-coating of NOA 61 on the half-ball lens (BK7; Edmund Optics). The half-ball lens was then aligned on the aperture using an automated centring machine, and NOA 61 was cured by ultraviolet irradiation to fix the half-ball lens with the aperture. The space between the half-ball lens and the aperture was filled with NOA 61, and another half-ball lens was placed on the opposite side of the aperture and fixed by ultraviolet curing of the NOA 61. The shell lenses (SF16) were pre-fabricated by a direct single-point diamond turning method with post-polishing. NOA 61 was then drop-coated on the half-ball lens, the shell lens was placed on the half-ball lens, and the half-ball lens and the shell lens were fixed by ultraviolet curing of the NOA 61. The ledge on the aperture allowed precise alignment between the aperture and the shell lens. The surface profile of the aperture and the shell lens is shown in Supplementary Fig. 34. The surface profiles

were measured using a non-contacting 3D surface profile measurement device (NH-3SPs, Mitaka Kohki). Repeating the same procedure (assembling another shell lens on the other side of the aperture) completed the fabrication of the monocentric lens.

Fabrication and characterization of the h-SiNR-PDA. Fabrication of the h-SiNR-PDA began with spin-coating of a polystyrene (PS) microsphere (diameter of 0.5 μm ; Thermo Fisher Scientific) solution on a silicon-on-insulator wafer (1.25- μm -thick top silicon; SOITEC). A series of dry etching processes with oxygen and SF_6 formed the SiNR textured surface⁴⁴. The residual PS microspheres were removed by sonication and piranha solution treatment. A series of doping processes were performed by using spin-on dopants. The SiNR nanomembrane was spin-coated with n-type spin-on-dopant (P509 solution; Filmtronics) and annealed at 200 °C for 15 min and at 975 °C for 12 min for n-doping, and then was spin-coated with the p-type spin-on dopant (B153 solution; Filmtronics) and annealed at 200 °C for 15 min and at 975 °C for 30 min for p-doping. The doping profiles were analysed by magnetic sector secondary ion mass spectrometry (IMS 7f, CAMECA; Supplementary Fig. 35). The nanorod-textured and doped silicon nanomembrane was transfer-printed onto the polyimide (PI) bottom substrate film (~1 μm thick; Sigma Aldrich) spin-coated on a SiO_2 wafer. The active silicon diode region was isolated using photolithography and dry etching, then the Al_2O_3 passivation layer (~25 nm) was deposited by the plasma-enhanced atomic layer deposition and isolated through photolithography and wet etching using a buffered oxide etchant. An additional PI film for the first intermediate dielectric (~1 μm thick) was spin-coated and cured. The via was patterned by photolithography and dry etching, and Cr/Au layers for first metal electrode (10/100 nm) were deposited and patterned by thermal evaporation and wet etching, respectively. Additional spin-coating and curing of the PI film for the second intermediate dielectric (~1 μm thick) and deposition of Cr/Au layers for the second metal electrode (10/100 nm) were performed using the same process. A final PI film for top encapsulation (~1 μm thick) was spin-coated and cured, then the entire PI film was etched into a hexagonal mesh structure by dry etching. The fabricated h-SiNR-PDA was detached from the SiO_2 wafer using a water-soluble tape (3M Corp.) and transfer-printed onto a hemispherically curved substrate made of polydimethylsiloxane (Dow Corning).

The individual pixel, that is, a photodiode serially connected to a blocking diode (lateral n-p-n configuration), was used for characterization. A white light-emitting diode was used as a light source. For device characterization, the photocurrents of the experimental and control devices (for example, the SiNR photodiode with and without Al_2O_3 passivation) were measured using a parameter analyser (B1500A, Agilent). Outlier data (the largest and smallest) were excluded.

Data availability

The data that support the plots within this paper and other findings of this study are available from the corresponding author upon reasonable request.

Code availability

The source codes for Matlab are available from the corresponding authors upon request.

Received: 29 November 2019; Accepted: 28 May 2020;

Published online: 22 June 2020

References

- Floreano, D. & Wood, R. J. Science, technology and the future of small autonomous drones. *Nature* **521**, 460–466 (2015).
- Jang, H. S. et al. A bezel-less tetrahedral image sensor formed by solvent-assisted plasticization and transformation of an acrylonitrile butadiene styrene framework. *Adv. Mater.* **30**, 1801256 (2018).
- Lee, G. J., Choi, C., Kim, D.-H. & Song, Y. M. Bioinspired artificial eyes: optic components, digital cameras and visual prostheses. *Adv. Funct. Mater.* **28**, 1705202 (2018).
- Chung, T. et al. Mining the smartness of insect ultrastructures for advanced imaging and illumination. *Adv. Funct. Mater.* **28**, 1705912 (2018).
- Lee, G. J., Nam, W. I. & Song, Y. M. Robustness of an artificially tailored fisheye imaging system with a curvilinear image surface. *Opt. Laser Technol.* **96**, 50–57 (2017).
- Zhou, F. et al. Optoelectronic resistive random access memory for neuromorphic vision sensors. *Nat. Nanotechnol.* **14**, 776–782 (2019).
- Lee, W. et al. Two-dimensional materials in functional three-dimensional architectures with applications in photodetection and imaging. *Nat. Commun.* **9**, 1417 (2018).
- Tsai, W.-L. et al. Band tunable microcavity perovskite artificial human photoreceptors. *Adv. Mater.* **31**, 1900231 (2019).
- Choi, C. et al. Human eye-inspired soft optoelectronic device using high-density MoS_2 -graphene curved image sensor array. *Nat. Commun.* **8**, 1664 (2017).
- Zhang, K. et al. Origami silicon optoelectronics for hemispherical electronic eye systems. *Nat. Commun.* **8**, 1782 (2017).
- Ko, H. C. et al. A hemispherical electronic eye camera based on compressible silicon optoelectronics. *Nature* **454**, 748–753 (2008).
- Artal, P. Optics of the eye and its impact in vision: a tutorial. *Adv. Opt. Photon.* **6**, 340–367 (2014).
- Song, Y. M. et al. Digital cameras with designs inspired by the arthropod eye. *Nature* **497**, 95–99 (2013).
- Floreano, D. et al. Miniature curved artificial compound eyes. *Proc. Natl Acad. Sci. USA* **110**, 9267–9272 (2013).
- Jeong, K.-H., Kim, J. & Lee, L. P. Biologically inspired artificial compound eyes. *Science* **312**, 557–561 (2006).
- Huang, C.-C. et al. Large-field-of-view wide-spectrum artificial reflecting superposition compound eyes. *Small* **10**, 3050–3057 (2014).
- Jagger, W. S. & Sands, P. J. A wide-angle gradient index optical model of the crystalline lens and eye of the rainbow trout. *Vis. Res.* **36**, 2623–2639 (1996).
- Jagger, W. S. & Sands, P. J. A wide-angle gradient index optical model of the crystalline lens and eye of the octopus. *Vis. Res.* **39**, 2841–2852 (1999).
- Mass, A. M. & Supin, A. Y. Adaptive features of aquatic mammals' eye. *Anat. Rec.* **290**, 701–715 (2007).
- Charman, W. N. & Tucker, J. The optical system of the goldfish eye. *Vis. Res.* **13**, 1–8 (1973).
- Ott, M. Visual accommodation in vertebrates: mechanisms, physiological response and stimuli. *J. Comp. Physiol. A* **192**, 97–111 (2006).
- Wagner, H.-J., Fröhlich, E., Negishi, K. & Collin, S. P. The eyes of deep-sea fish. II. Functional morphology of the retina. *Prog. Retin. Eye Res.* **17**, 637–685 (1998).
- Partridge, J. C., Archer, S. N. & Lythgoe, J. N. Visual pigments in the individual rods of deep-sea fishes. *J. Comp. Physiol. A* **162**, 543–550 (1988).
- Wu, T. et al. Design and fabrication of silicon-tessellated structures for monocentric imagers. *Microsyst. Nanoeng.* **2**, 16019 (2016).
- Liu, H. W., Huang, Y. & Jiang, H. Artificial eye for scotopic vision with bioinspired all-optical photosensitivity enhancer. *Proc. Natl Acad. Sci. USA* **113**, 3982–3985 (2016).
- Zukauskas, A. et al. Tuning the refractive index in 3D direct laser writing lithography: towards GRIN microoptics. *Laser Photon. Rev.* **9**, 706–712 (2015).
- Yu, N. & Capasso, F. Flat optics with designer metasurfaces. *Nat. Mater.* **13**, 139–150 (2014).
- Steel, W. H. On the choice of glasses for cemented achromatic aplanatic doublets. *Aust. J. Phys.* **7**, 244–253 (1954).
- Lee, W. et al. High-resolution spin-on-patterning of perovskite thin films for a multiplexed image sensor array. *Adv. Mater.* **29**, 1702902 (2017).
- Sim, K. et al. Three-dimensional curvy electronics created using conformal additive stamp printing. *Nat. Electron.* **2**, 471–479 (2019).
- Shin, G. et al. Micromechanics and advances designs for curved photodetector arrays in hemispherical electronic-eye cameras. *Small* **6**, 851–856 (2010).
- Huang, Z. et al. Three-dimensional integrated stretchable electronics. *Nat. Electron.* **1**, 473–480 (2018).
- Park, S.-I. et al. Theoretical and experimental studies of bending of inorganic electronic materials on plastic substrates. *Adv. Funct. Mater.* **18**, 2673–2684 (2008).
- Choi, M. K. et al. Wearable red-green-blue quantum dot light-emitting diode array using high-resolution intaglio transfer printing. *Nat. Commun.* **6**, 7149 (2015).
- Kim, J. et al. Stretchable silicon nanoribbon electronics for skin prosthesis. *Nat. Commun.* **5**, 5747 (2014).
- Rim, S.-B., Catrysse, P. B., Dinyari, R., Huang, K. & Peumans, P. The optical advantages of curved focal plane arrays. *Opt. Express* **16**, 4965–4971 (2008).
- Sheng, X., Johnson, S. G., Michel, J. & Kimerling, L. C. Optimization-based design of surface textures for thin-film Si solar cells. *Opt. Express* **19**, A841–A850 (2011).
- Sheng, X. et al. Printing-based assembly of quadruple-junction four-terminal microscale solar cells and their use in high-efficiency modules. *Nat. Mater.* **13**, 593–598 (2014).
- Hoang, N.-V. et al. Giant enhancement of luminescence down-shifting by a doubly resonant rare-earth-doped photonic metastructure. *ACS Photonics* **4**, 1705–1712 (2017).
- Savin, H. et al. Black silicon solar cells with interdigitated back-contacts achieve 22.1% efficiency. *Nat. Nanotechnol.* **10**, 624–628 (2015).
- Gao, Y. et al. Photon-trapping microstructures enable high-speed high-efficiency silicon photodiodes. *Nat. Photon.* **11**, 301–308 (2017).
- Lucovsky, G., Schwarz, R. F. & Emmons, R. B. Transit-time considerations in p-i-n diodes. *J. Appl. Phys.* **35**, 622–628 (1964).
- Kyomasu, Mikio Development of an integrated high speed silicon PIN photodiode sensor. *IEEE Trans. Electron Devices* **42**, 1093–1099 (1995).
- Gao, M., Cho, M., Han, H.-J., Jung, Y. S. & Park, I. Palladium-decorated silicon nanomesh fabricated by nanosphere lithography for high performance, room temperature hydrogen sensing. *Small* **14**, 1703691 (2018).

Acknowledgements

This research was supported by the Institute for Basic Science (IBS-R006-A1). This research was also supported by the National Research Foundation (NRF) of Korea (2017M3D1A1039288/2018R1A4A1025623).

Author contributions

Min Sung Kim, G.J.L., C.C., Min Seok Kim, K.W.C., Y.M.S. and D.-H.K. designed the experiments, analysed the data and wrote the paper. Min Sung Kim, C.C., M.L., H.C. and M.K.C. fabricated the photodiode array and performed characterization of individual devices. G.J.L., Min Seok Kim and H.M.K. performed theoretical analysis on optics. S.L. and N.L. performed theoretical analysis on mechanics. All authors discussed the results and commented on the manuscript.

Competing interests

The authors declare no competing interests.

Additional information

Supplementary information is available for this paper at <https://doi.org/10.1038/s41928-020-0429-5>.

Correspondence and requests for materials should be addressed to Y.M.S. or D.-H.K.

Reprints and permissions information is available at www.nature.com/reprints.

Publisher's note Springer Nature remains neutral with regard to jurisdictional claims in published maps and institutional affiliations.

© The Author(s), under exclusive licence to Springer Nature Limited 2020

In the format provided by the authors and unedited.

An aquatic-vision-inspired camera based on a monocentric lens and a silicon nanorod photodiode array

Min Sung Kim^{1,2,7}, Gil Ju Lee^{3,7}, Changsoon Choi^{1,2,7}, Min Seok Kim^{3,7}, Mincheol Lee^{1,2}, Siyi Liu⁴, Kyoung Won Cho^{1,2}, Hyun Myung Kim³, Hyojin Cho^{1,2}, Moon Kee Choi⁵, Nanshu Lu⁴, Young Min Song³✉ and Dae-Hyeong Kim^{1,2,6}✉

¹Center for Nanoparticle Research, Institute for Basic Science (IBS), Seoul, Republic of Korea. ²School of Chemical and Biological Engineering, Institute of Chemical Processes, Seoul National University, Seoul, Republic of Korea. ³School of Electrical Engineering and Computer Science, Gwangju Institute of Science and Technology, Gwangju, Republic of Korea. ⁴Center for Mechanics of Solids, Structures and Materials, Department of Aerospace Engineering and Engineering Mechanics, Department of Biomedical Engineering, Texas Materials Institute, University of Texas at Austin, Austin, TX, USA. ⁵School of Materials Science and Engineering, Ulsan National Institute of Science and Technology (UNIST), Ulsan, Republic of Korea. ⁶Department of Materials Science and Engineering, Seoul National University, Seoul, Republic of Korea. ⁷These authors contributed equally: Min Sung Kim, Gil Ju Lee, Changsoon Choi, Min Seok Kim. ✉e-mail: ymsong@gist.ac.kr; dkim98@snu.ac.kr

Supplementary Information

An aquatic vision inspired camera based on a monocentric lens and a silicon nanorod photodiode array

Min Sung Kim^{1,2†}, Gil Ju Lee^{3†}, Changsoon Choi^{1,2†}, Min Seok Kim^{3†}, Mincheol Lee^{1,2}, Siyi Liu⁴, Kyoung Won Cho^{1,2}, Hyun Myung Kim³, Hyojin Cho^{1,2}, Moon Kee Choi⁵, Nanshu Lu⁴, Young Min Song^{3*}, and Dae-Hyeong Kim^{1,2,6*}

¹*Center for Nanoparticle Research, Institute for Basic Science (IBS), Seoul 08826, Republic of Korea.*

²*School of Chemical and Biological Engineering, Institute of Chemical Processes, Seoul National University, Seoul 08826, Republic of Korea.*

³*School of Electrical Engineering and Computer Science, Gwangju Institute of Science and Technology, Gwangju 61005, Republic of Korea.*

⁴*Center for Mechanics of Solids, Structures and Materials, Department of Aerospace Engineering and Engineering Mechanics, Department of Biomedical Engineering, Texas Materials Institute, University of Texas at Austin, Austin, TX 78712, USA.*

⁵*School of Materials Science and Engineering, Ulsan National Institute of Science and Technology (UNIST), Ulsan 44919, Republic of Korea.*

⁶*Department of Materials Science and Engineering, Seoul National University, Seoul 08826, Republic of Korea.*

[†]*M. S. Kim, G. J. Lee, C. Choi, and M. S. Kim contributed equally to this work.*

^{*}*To whom correspondences should be addressed.*

E-mail: dkim98@snu.ac.kr and ymsong@gist.ac.kr

Supplementary Notes

Supplementary Note 1. Optical simulations for the aquatic eye in nature

Three-dimensional ray-tracing simulations based on the Monte-Carlo method were performed using commercial software (OpticStudio 16.0, Radiant ZEMAX LLC, USA). The optical model of the aquatic eye consists of the protruding monocentric lens with the parabolic refractive index (RI) distribution ranging from 1.377 to 1.540, the cornea with the RI of 1.33, the iris with $F/\#$ of 0.9, and the retina with a hemispherical shape (Supplementary Fig. 4). By receiving the light from a point source, the protruding monocentric lens forms a small focal spot, whose radius is 16.9 μm , 23.1 μm , and 20.9 μm for the light from 0° , 40° , and 80° (*i.e.*, FoV is 160°), respectively (Fig. 1c). Such small focal spot radii that support the small coma aberration are due to the parabolic RI distribution as well as the spherical lens shape. In comparison, the spherical lens with the homogeneous RI distribution forms large focal spots, whose radius is 23.4 μm , 62.5 μm , and 62.7 μm for the light from 0° , 40° , and 80° (*i.e.*, same angle conditions with the parabolic RI distribution case but much larger focal spot radii with the homogeneous RI distribution), respectively.

Supplementary Note 2. Design optimisation of the monocentric lens

For the systematic design optimisation of the monocentric lens, we exploited the automatic optimisation process included in the commercial software (OpticStudio 16.0). The optimisation process began with setting the initial geometric values of the lenses and aperture. Considering the facile lens fabrication and optimisation, we set the number of lenses as two. The inner lens was set to the commercial half-ball lens (BK7, radius = 1 mm). The material of the outer lens was selected as BK7 for an initial material. The distance between lenses was

fixed as zero to remove the optical alignment. The thickness and radius of the aperture were fixed as 0.5 mm and 1 mm, respectively. In addition, we predesignated the distance from the monocentric lens to the image plane and the radius of curvature (RoC) of the image plane as 10 mm and 10 mm, respectively. Then, the parameters (*e.g.*, material, radius, thickness of outer lens, distance to the image plane, and RoC of the image plane) were optimised through the global optimisation process to minimise optical aberrations at the wavelength of 480 nm, 546 nm, and 644 nm.

We investigated the focusing capability (*e.g.*, focal spot radius) depending on the RI of individual lenses. Since the aquatic-vision-inspired camera operates under air, not underwater, the RI distribution of the monocentric lens should be optimised differently from that of the protruding monocentric lens. Therefore, we compared two different kinds of the lens configuration. One is a spherical doublet lens in which the RI of the outer shell is smaller than that of the inner core ($n_{in} > n_{out}$; Supplementary Fig. 9a), and the other is a spherical doublet lens in which the RI of the outer shell is larger than that of the inner core ($n_{in} < n_{out}$; Supplementary Fig. 9b). Among them, the latter lens forms much smaller focal spot radii for all incident angles compared to the former one (Supplementary Fig. 9c), which suggests that the outer shell with a large RI and the inner core with a small RI are optimal for the panoramic imaging under air. The focal spot radii of the monocentric lens ($n_{in} < n_{out}$) are much smaller than those of the homogeneous ball lens ($n_{in} = n_{out}$).

The focal spot radius depends on the RI difference of the core-shell structure ($\Delta n = n_{out} - n_{in}$) (Supplementary Fig. 10a). Based on optical simulations, small Δn leads to small correction of the optical aberration and large Δn leads to excessive refraction. Thereby, the large focal spot radius is formed in both cases (*i.e.*, small and large Δn). The optimised Δn is

around 0.13, and thus BK7 and SF16 were used as an inner half-ball lens and an outer shell lens because their RI values are 1.52 (n_{in}) and 1.65 (n_{out}), respectively.

In addition, the focusing capability is also strongly dependent on the dimension of each lens, such as the ratio of the lens radius (R_{in}/R_{out}) (Supplementary Fig. 10b). When R_{in}/R_{out} is 0.48, the smallest spot radius is formed, which is much smaller than that formed by the homogeneous spherical lens of BK7 and SF16. Therefore, the radius of BK7 (R_{in}) and SF16 (R_{out}) is designed to be 2 mm and 4.1 mm, respectively.

The aperture position is also crucial to achieve the aberration-free wide FoV imaging without vignetting because the aperture blocks the oblique incident lights. Based on optical simulations, the front aperture blocks the incident lights over 30° and the rear aperture blocks the incident lights over 20° (Supplementary Fig. 11a left and right, respectively), leading to the large light intensity attenuation at wide angles. In contrast, the center aperture can minimise the optical loss by the aperture (Supplementary Fig. 11a middle), and thus a clear image with small vignetting can be obtained by the monocentric lens with the center aperture.

The monocentric lens (Supplementary Table 1) that is systematically optimised for the ambient condition shows the better focusing capability than the natural protruding monocentric lens in the aquatic eye (Supplementary Fig. 12). Although the protruding monocentric lens with full aperture can gather a large amount of light, which is helpful in the dim underwater environment, its focusing capability is degraded due to the large aperture size. Furthermore, our monocentric lens with two RI values formed comparable (or smaller in some conditions) focal spots to those formed by the protruding monocentric lens with a parabolic RI profile and the monocentric lens with three RI values, although the focal spot radius at wide FoV (120°) slightly increases (Supplementary Fig. 12). In the optical simulations, all geometrical parameters except the RI profile were set to be same in the optical systems for fair comparison.

The distances between each lens and image plane were optimised for the FoV of 120°. The parabolic RI profile of the protruding monocentric lens is referred from the previous report^{S5}. The optical information for individual components of the lens was referred from the library in the commercial software (OpticStudio 16.0), and the optical information of NOA 61 was referred from its technical sheet^{S6}. The detailed information of the lens components of the monocentric lens with three RI values is described in Supplementary Table 2. In addition, the monocentric lens with two RI values is advantageous for the lens fabrication in terms of the manufacturing difficulty and cost. The comparison of specifications between those monocentric lenses are summarised in Supplementary Table 3.

Supplementary Note 3. Calculation of optical aberration coefficients

The monochromatic spot radius (Fig. 2f) and Seidel aberration coefficients (Fig. 2g) of each optical system were calculated using the commercial software (OpticStudio 16.0). The monocentric lens (Supplementary Table 1) was compared with control lenses, *i.e.*, the conventional wide angle multi-lens (Supplementary Table 4) and the homogeneous ball lens (Supplementary Table 5). The aperture size of each optical system is set to be same. The monochromatic spot radius formed by the monocentric lens is maintained as $\sim 4 \mu\text{m}$ for all incident angles, while that by the wide angle multi-lens increases to $13.2 \mu\text{m}$ at wide angles and that by the homogeneous ball lens is always larger than $14.5 \mu\text{m}$.

Next, various optical aberrations of the monocentric lens are drastically reduced due to its spherical shape and core-shell structure as well as integration with the *h-SiNR*-PDA^{S7}. The spherical shape of monocentric lens and its integration with the *h-SiNR*-PDA reduce off-axis achromatic aberrations such as COMA and ASTI. The on-axis achromatic aberration (*e.g.*, SPHA) is also reduced due to the short optical path as the small refraction of the inner core

with low RI compensates the large refraction of the outer shell with high RI. Furthermore, the chromatic aberrations (*e.g.*, CTA and CLA) as well as achromatic aberrations (*e.g.*, SPHA, COMA, and ASTI) are corrected due to the different RI dispersion in the core-shell structure of the monocentric lens. Therefore, the coefficients of SPHA, COMA, ASTI, CTA, and CLA of the monocentric lens were 6.02×10^{-3} , 1.05×10^{-3} , 7.90×10^{-5} , 4.30×10^{-4} , and 3.14×10^{-4} , respectively. On the other hand, the coefficients of SPHA, COMA, ASTI, CTA, and CLA of the wide angle multi-lens were 8.33×10^{-3} , 5.97×10^{-3} , 7.02×10^{-3} , 4.91×10^{-3} , and 2.62×10^{-3} , respectively. And the coefficients of SPHA, COMA, ASTI, CTA, and CLA of the homogeneous ball lens were 1.42×10^{-2} , 4.06×10^{-3} , 2.40×10^{-3} , 1.51×10^{-3} , and 4.77×10^{-3} , respectively.

Supplementary Note 4. Mechanical analysis on the hemispherical silicon nanorod photodiode array

The process of attaching the *h-SiNR*-PDA to the hemispherical substrate was simulated by using the commercial software (ABAQUS). According to the finite element analysis (FEA), the *h-SiNR*-PDA was conformally attached onto the concavely hemispherical substrate whose radius is 7.5 mm. The tangential interaction between the *h-SiNR*-PDA and the hemispherical substrate was frictional, and the friction coefficient was set to be 0.05. The normal interaction was a hard contact, and no separation was assumed after the contact. The hemispherical substrate was assumed to be analytically rigid to improve the accuracy of the interaction. Both four-node and three-node shell elements were used to model the *h-SiNR*-PDA. A homogeneous shell was used to model the serpentine interconnections without metal electrodes, while a composite shell was used to model the serpentine interconnections with metal electrodes and the photodiodes. To simplify the computation, only the gold layer ($E_{Au} = 77.2$ GPa, $\nu_{Au} = 0.42$), the silicon layer ($E_{Si} = 79.4$ GPa, $\nu_{Si} = 0.22$), and the PI layer ($E_{PI} = 2.5$ GPa, $\nu_{PI} = 0.34$) were

considered in the simulation. Based on the FEA, the maximum strain induced on the silicon layer (ϵ_{Si}), the gold layer (ϵ_{Au}), and the PI layer (ϵ_{PI}) were calculated and plotted in Fig. 3c.

Supplementary Note 5. Optical simulations for light trapping by silicon nanorods

The three-dimensional rigorous coupled wave analysis (RCWA) and finite-difference time-domain (FDTD) method were applied by using commercial software (RSoft Design Group, USA) to engineer the structural parameters of *SiNR* (e.g., height and period). The fifth diffraction order and 0.2 nm grid size were used in the RCWA to calculate the optical efficiency, which was sufficient to numerically stabilise the results. In the FDTD simulation, the identical grid size was exploited. The electric field distributions and absorption profiles were simulated by the FDTD. The material dispersion and extinction coefficients for Si, which were found in the library of the software, were adopted for obtaining exact outputs. Matlab (Mathworks, USA) was used to reconstruct three-dimensional absorption profiles.

The electric field distribution of the bare silicon and the *SiNR* is shown in Supplementary Fig. 23. At short wavelength (*i.e.*, 430 nm), the electric fields are rapidly extinct at the shallow depth for both cases. At long wavelength (*i.e.*, 670 nm), most light penetrates the bare silicon membrane of 1.25 μm thickness. On the other hand, the light is diffracted by the *SiNR* structure and trapped inside the *SiNR* membrane due to the multiple total internal reflections, which is confirmed by evanescent fields. Such a light trapping effect enhances the photo-absorption efficiency.

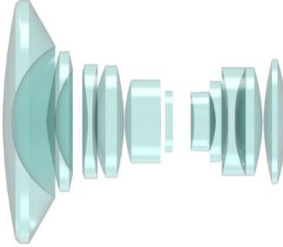
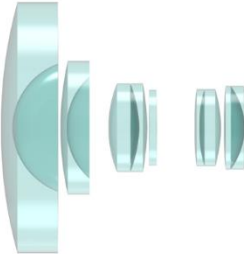
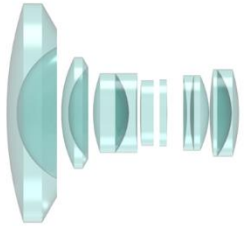
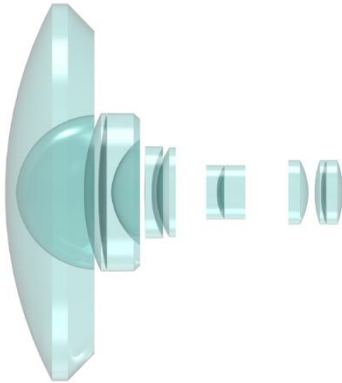
Supplementary Note 6. Imaging demonstration setup for the aquatic-vision-inspired camera

The optical camera image of the imaging demonstration setup is shown in

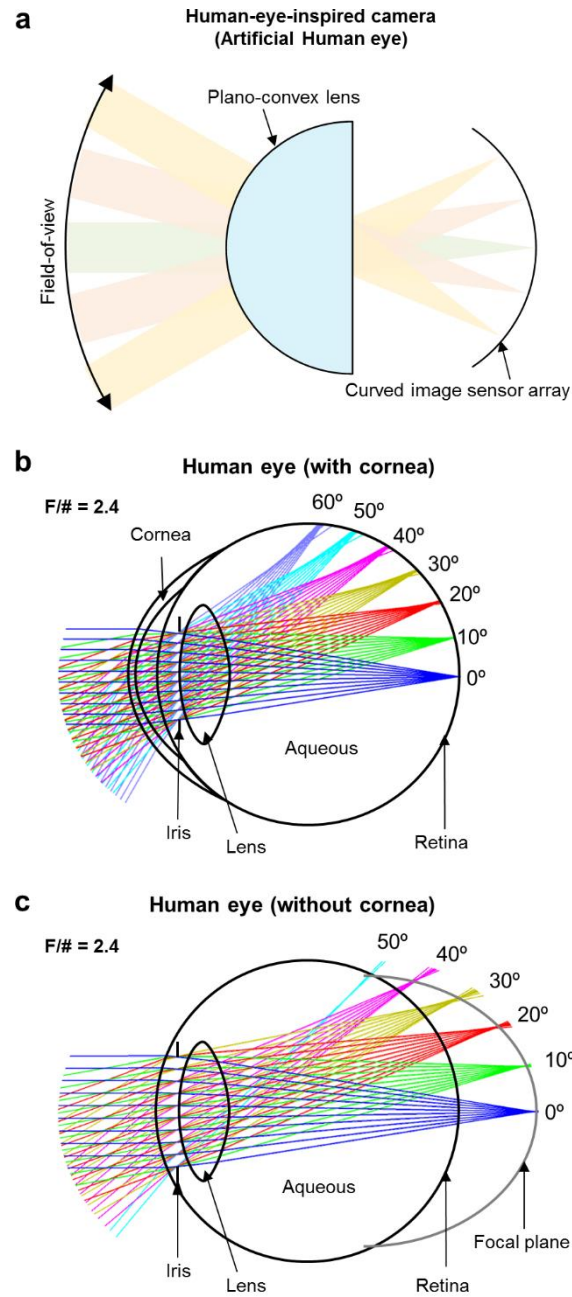
Supplementary Fig. 29. A dome-shaped diffusive light source (MB-DL306, Metaphase Technologies Inc., USA) offered the uniform white light illumination, and the mounted mask fabricated by a 3D printer (Ultimaker 3, Ultimaker, Netherlands) generated objects. A scanning process was employed to enhance the effective resolution, where the aquatic-vision-inspired camera was rotated from -7° to 7° and -5° to 5° in the horizontal and vertical direction with the increment of 0.7° and 0.5° , respectively. For the rotation stages, two motorised rotators (PR-50C, Newport, USA) were perpendicularly joined, and the customised frames were used to secure the radius of rotation. The motorised rotators were controlled by the motorisation stage controller (ESP7000, Newport, USA).

For the real-time signal readout, a high-speed digitiser, comprised of the analog to digital converter (ADC) chips and a field programmable gate array (FPGA) chip on a printed circuit board (PCB), was used for the data acquisition of the 23 by 23 pixels in the *h-SiNR*-PDA. Each pixel in the *h-SiNR*-PDA was connected to the digitiser via the ACF. A schematic circuit diagram showing the wiring is included in Supplementary Fig. 16. The digitiser (32 by 32 channels) worked as an interface board between the *h-SiNR*-PDA and the computer for acquiring the photocurrent information from individual photodiodes and transmitting the acquired data to the computer (Supplementary Fig. 30). The USB-based serial communication offered a data pathway between the computer and the digitiser. The FPGA processed the data with the 2GHz clock speed for real-time data digitalisation. All of these electronic units can be miniaturised by utilising an application specific integrated circuit (ASIC). Matlab was exploited to send command signals to the motorisation stage controller and the digitiser. The acquired photocurrent information was processed using Matlab, and the pixelated images were rendered on the hemispherical surface whose radius is same with the RoC of *h-SiNR*-PDA.

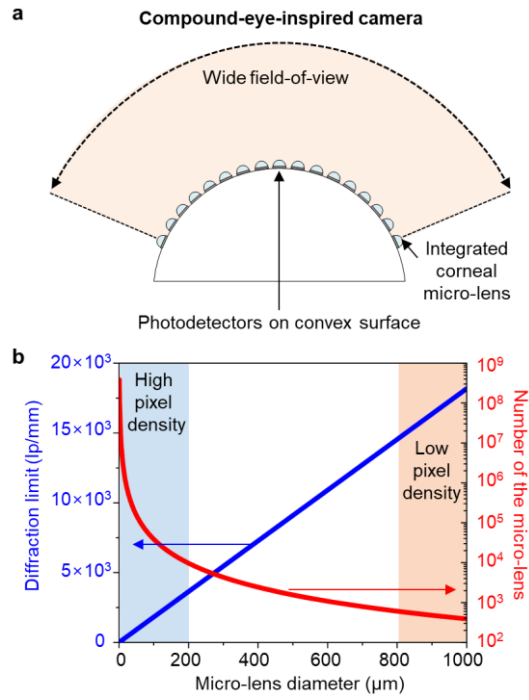
Supplementary Figures

Reference	Schematic of wide angle multi-lens optics	Parameters
[S1]		Number of lenses: 11 Length: 101.6 mm Maximum diameter: 58.2 mm Volume: 2,703 cm ³
[S2]		Number of lenses: 9 Length: 95.5 mm Maximum diameter: 59.5 mm Volume: 2,827 cm ³
[S3]		Number of lenses: 10 Length: 85.7 mm Maximum diameter: 50.4 mm Volume: 1,710 cm ³
[S4]		Number of lenses: 10 Length: 125 mm Maximum diameter: 90 mm Volume: 7,308 cm ³

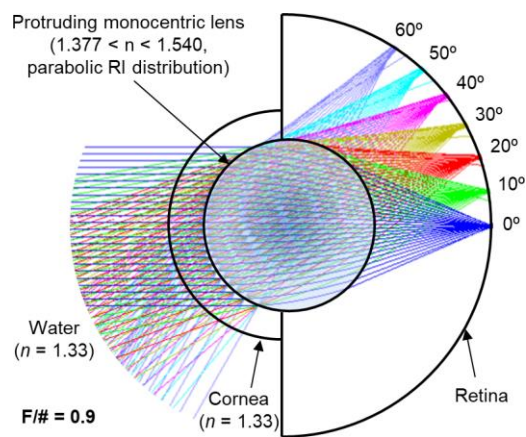
Supplementary Figure 1 | System construction, the number of lenses, dimension, and volume of the conventional wide angle multi-lens optics. Schematic illustration (left) and detailed parameters (right) of the conventional wide angle multi-lens optics.



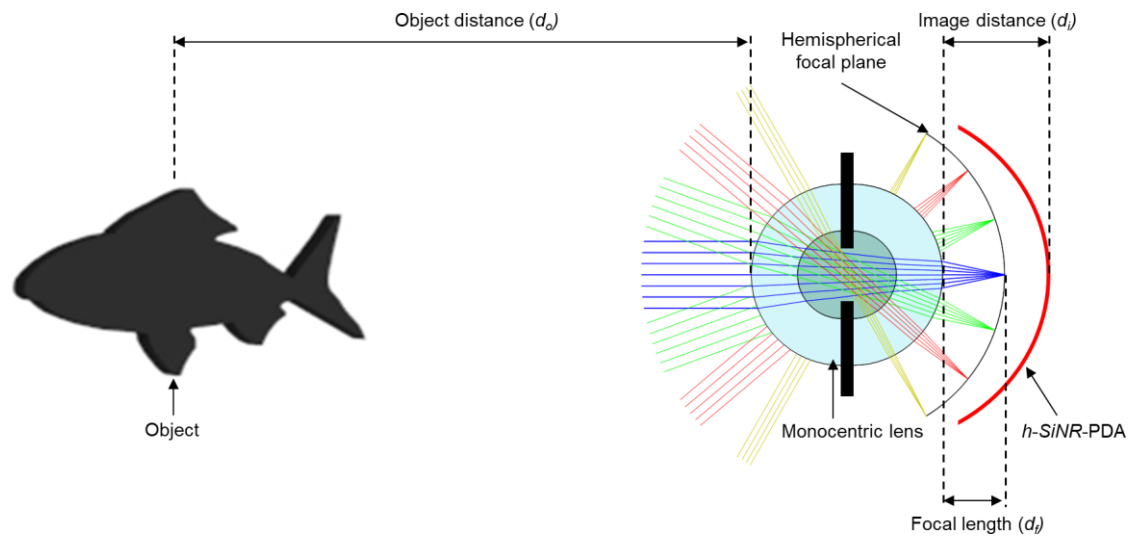
Supplementary Figure 2 | Optical analysis of a human-eye-inspired camera and a human eye. **a**, Human-eye-inspired camera based on a plano-convex lens and a curved image sensor array^{S8,S9}. **b,c**, Ray-tracing simulation for an optical model^{S10} of the human eye with the cornea (**b**) and without the cornea (**c**). The incident ray over 50° is blocked by the iris in the human eye without the cornea.



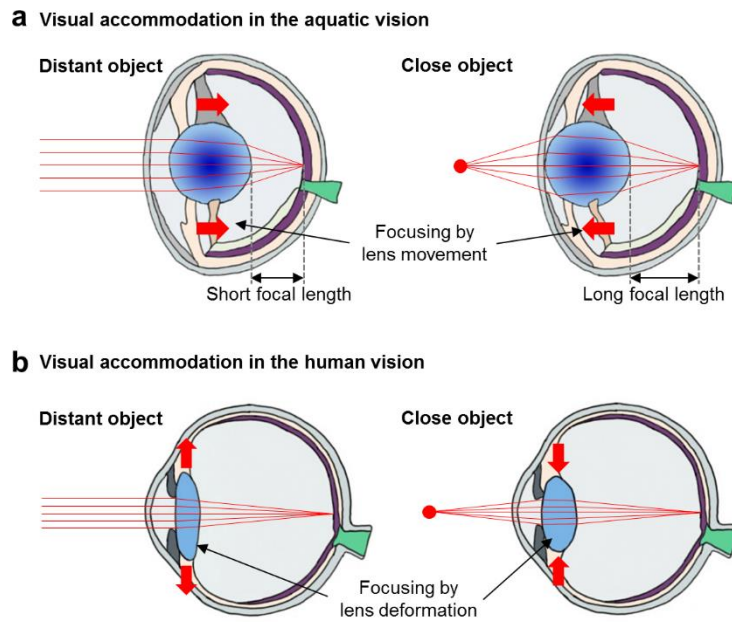
Supplementary Figure 3 | Schematic illustration and optical analysis of the compound-eye-inspired camera. **a**, Arthropod-inspired compound-eye-type camera using a convex-type array of the image sensor and micro-lens, in which each photodetector is integrated with a micro-lens^{S11}. **b**, Diffraction limit of the corneal micro-lens (left) and the number of the micro-lens (right) depending on its diameter. As the micro-lens diameter decreases, the pixel density is enhanced but the diffraction limit of the corneal micro-lens is reduced.



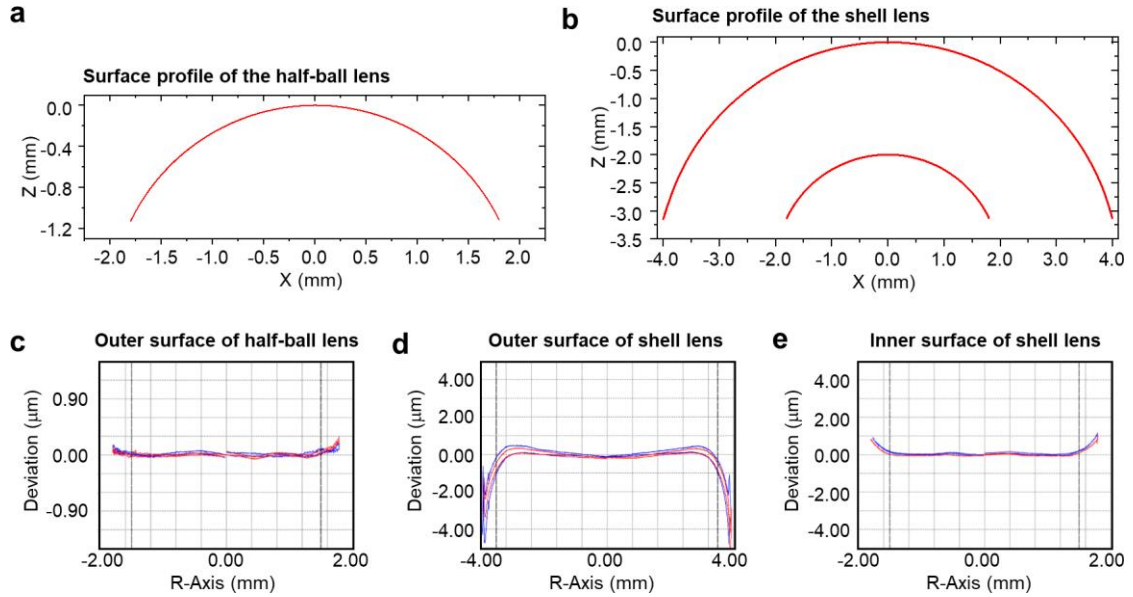
Supplementary Figure 4 | Ray-tracing simulation with a theoretical model of the aquatic eye. Ray tracing simulation for a protruding monocentric lens with the parabolic RI distribution. The parabolic RI distribution in the monocentric lens minimises optical aberrations caused by the high curvature of the monocentric lens and the optical dispersion. The RI of the background water is 1.33. The aperture is set to be $F/\# = 0.9$.



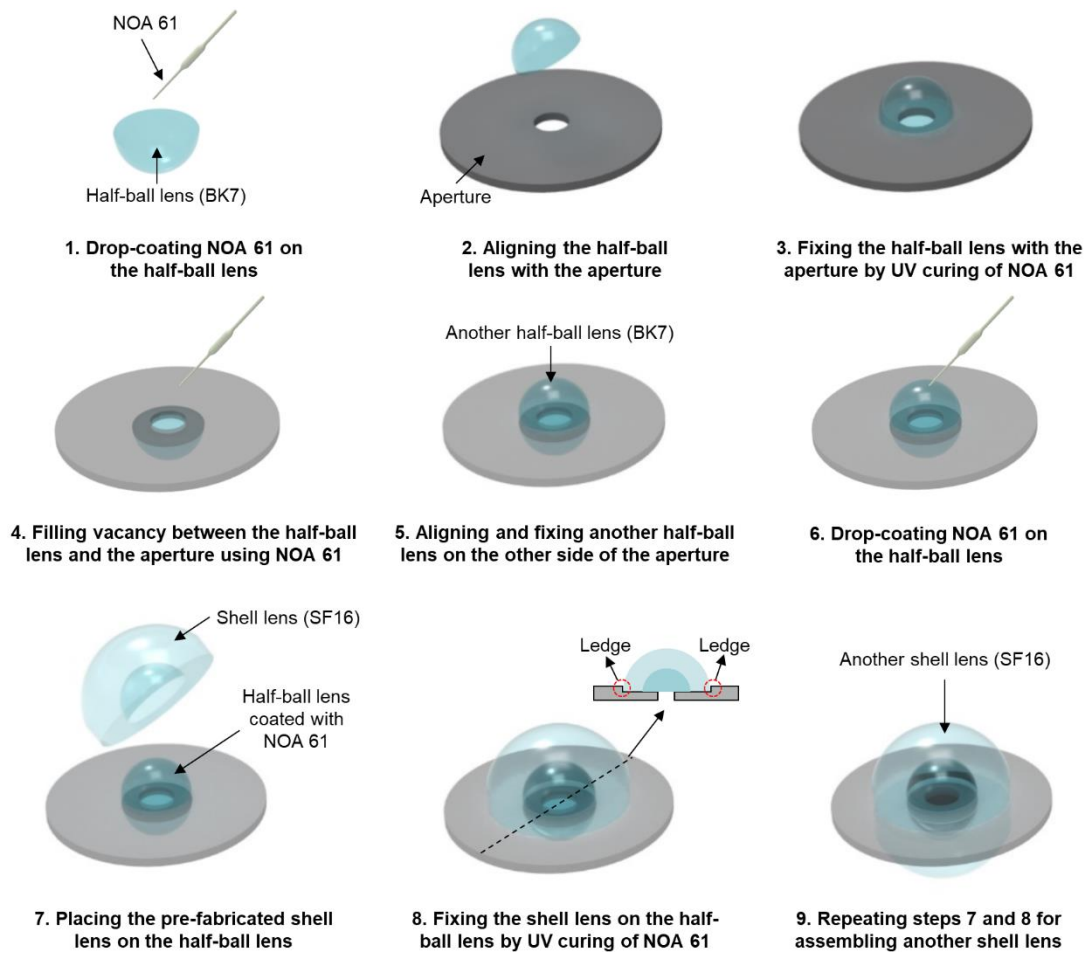
Supplementary Figure 5 | Imaging parameters. Schematic illustration showing imaging parameters, such as the object distance (d_o ; distance between the object and the monocentric lens), the image distance (d_i ; distance between the monocentric lens and the retina), and the focal length (d_f ; distance between the monocentric lens and the focal plane).



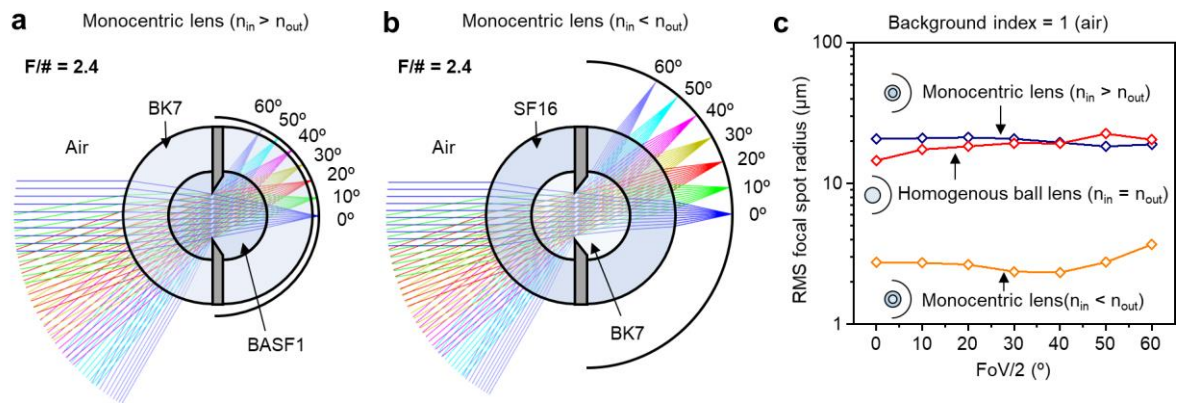
Supplementary Figure 6 | Comparison of the visual accommodation in the aquatic vision and the human vision. a, Visual accommodation in the aquatic eye by moving the protruding monocentric lens back and forth without changing the original lens shape. **b**, Visual accommodation in the human eye which requires the change of the lens shape.



Supplementary Figure 7 | Surface profiles and roughness of each lens. **a,b**, Surface profile of the half-ball lens (**a**) and the shell lens (**b**). **c-e**, Surface roughness of the outer surface of the half-ball lens (**c**), the outer surface of the shell lens (**d**), and the inner surface of the shell lens (**e**). Their best fit radii are 1.9998295 mm, 4.1014051 mm, and -2.0024906 mm, which are approximately 2 mm, 4.1 mm, and -2 mm, respectively. The RMS value of each roughness is 0.0265 μm , 0.2008 μm , and 0.5630 μm , respectively. The peak-to-peak variation of each roughness is 0.1665 μm , 1.5061 μm , and 0.2949 μm , respectively. The edge of the lens couldn't be observed due to the limitation of the measurement tool.

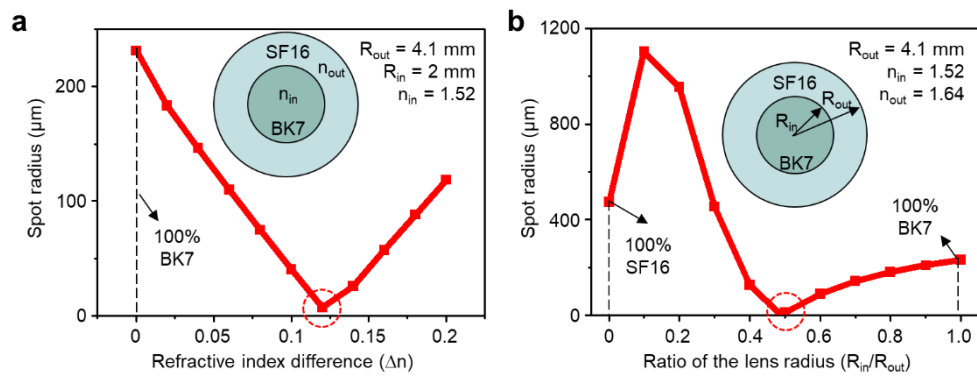


Supplementary Figure 8 | Fabrication of the monocentric lens. Schematic illustrations showing the fabrication process of the monocentric lens.

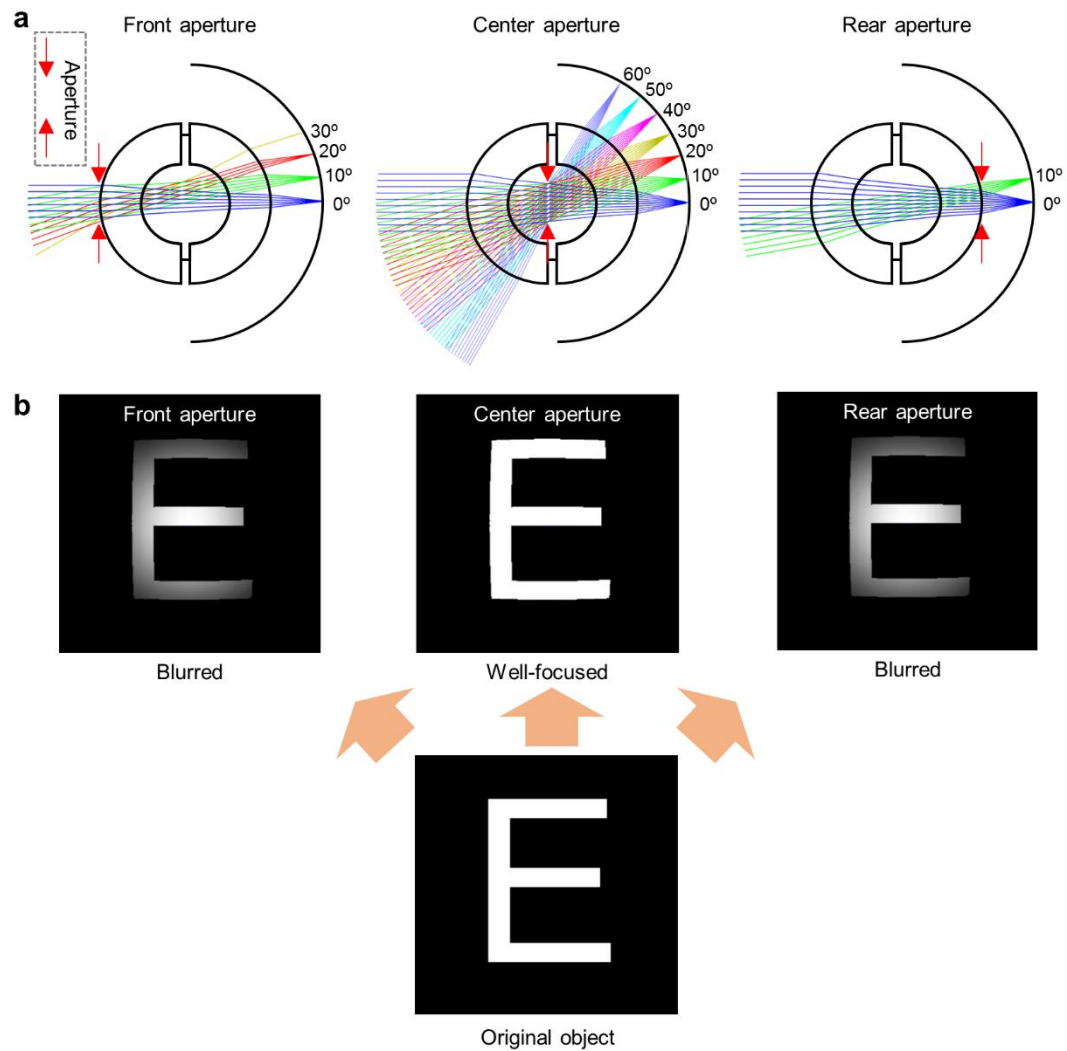


Supplementary Figure 9 | Focal spot radius depending on the relative size of n_{in} and n_{out} .

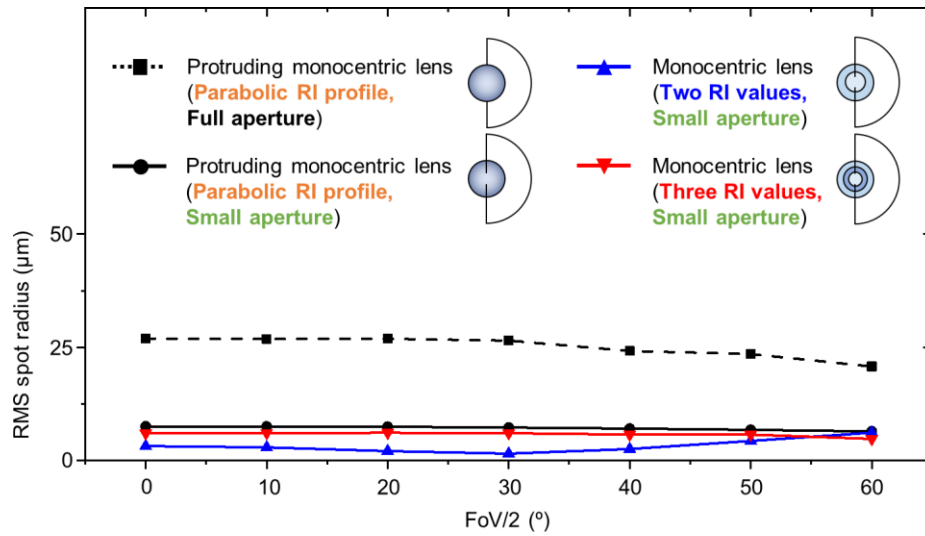
a,b, Ray tracing simulations for two artificial aquatic eyes with different RI distributions (*e.g.*, $n_{in} > n_{out}$ (**a**) and $n_{in} < n_{out}$ (**b**)). **c**, Root mean square (RMS) focal spot radius of the monocentric lens (*e.g.*, both case of $n_{in} > n_{out}$ and $n_{in} < n_{out}$) and the homogeneous ball lens (BK7; $n_{in} = n_{out}$) for the incident lights from various angles. When $n_{in} < n_{out}$, the smallest focal spots are formed.



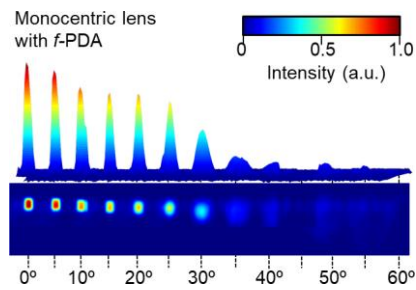
Supplementary Figure 10 | Optimised design factors of the monocentric lens. a,b, Optical simulation of the monochromatic spot radius for various RI differences (Δn) (**a**) and for various ratios of the inner and outer lens radius ($R_{\text{in}}/R_{\text{out}}$) (**b**).



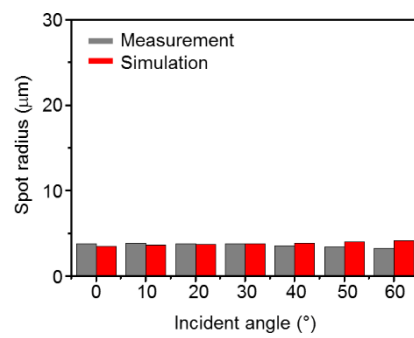
Supplementary Figure 11 | Optical simulations with various aperture positions. a,b, Ray-tracing simulations (a) and imaging simulations (b), in which the aperture is placed at different positions. The red arrows in the grey dashed box shows the symbol of the aperture. The model with the front or rear aperture position suffers from serious vignetting (*i.e.*, the incident light is blocked).



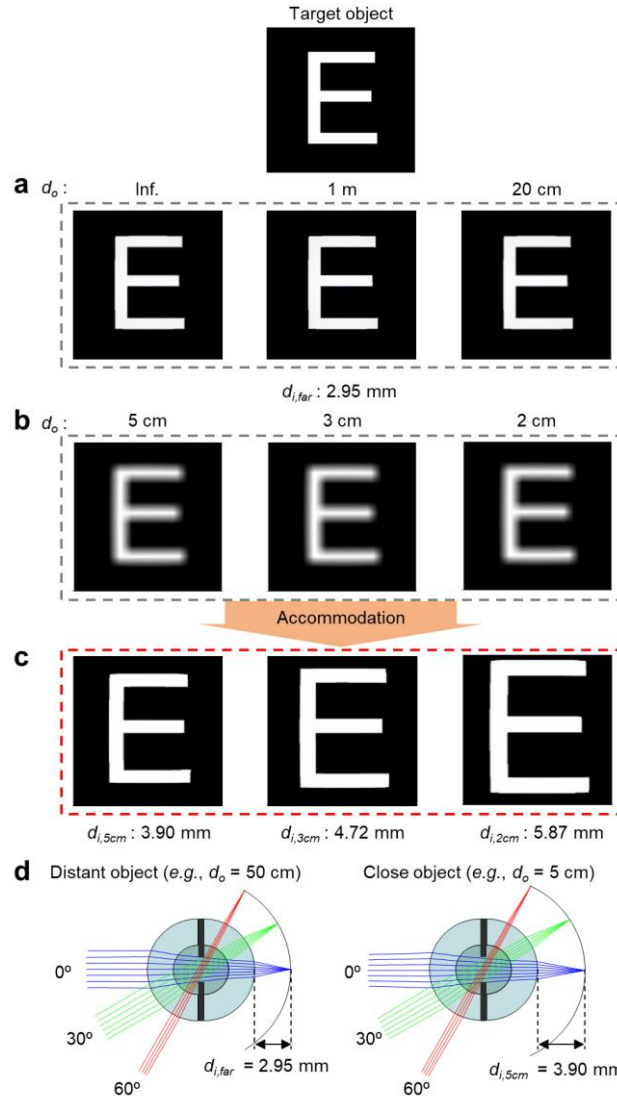
Supplementary Figure 12 | Simulation of the focal spot radius for various monocentric lens designs. The RMS spot radii for four kinds of monocentric lenses such as the natural protruding monocentric lens with the parabolic RI profile and a full aperture, the protruding monocentric lens with the parabolic RI profile and a small aperture, the monocentric lens with the parabolic RI profile and a small aperture, the monocentric lens with two RI values and a small aperture, the monocentric lens with three RI values and a small aperture.



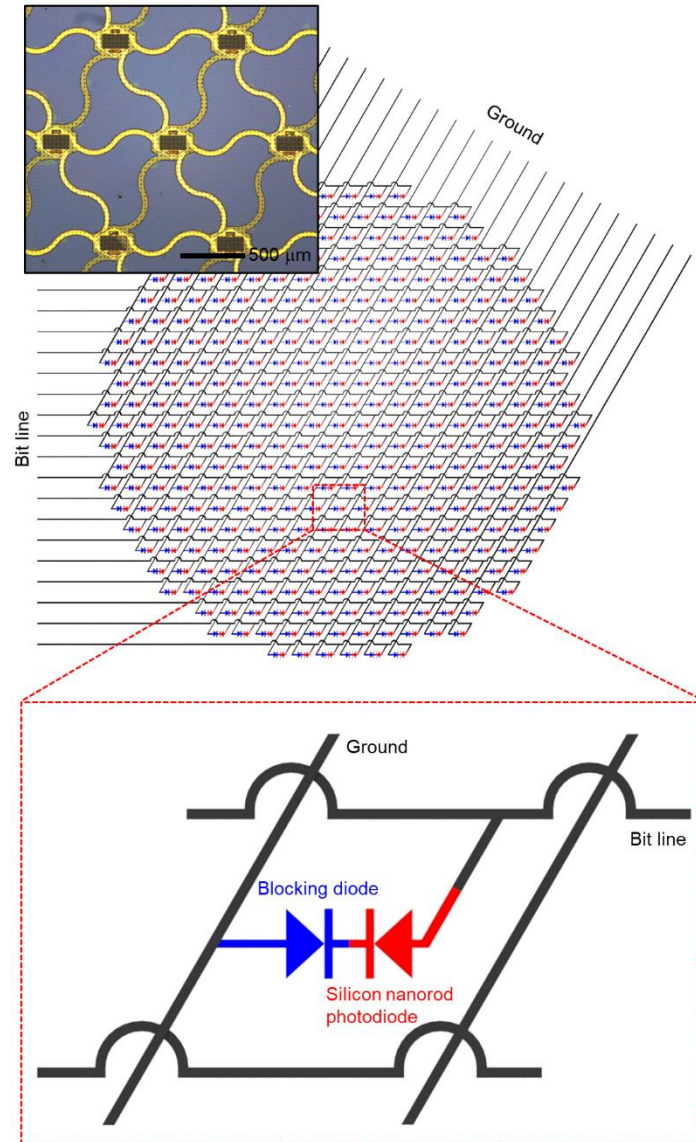
Supplementary Figure 13 | Light intensity and spot radius of the lights from various angles focused by the monocentric lens and detected with a flat photodetector array. Intensity (top) and size (bottom) of laser spots for different incident angles, which are focused by the monocentric lens and measured with the f -PDA.



Supplementary Figure 14 | Experimental and theoretical estimation of the radius of spots focused by the monocentric lens. The focal spot radius for different incident angles obtained through the experimental measurement (grey) and optical simulation (red).

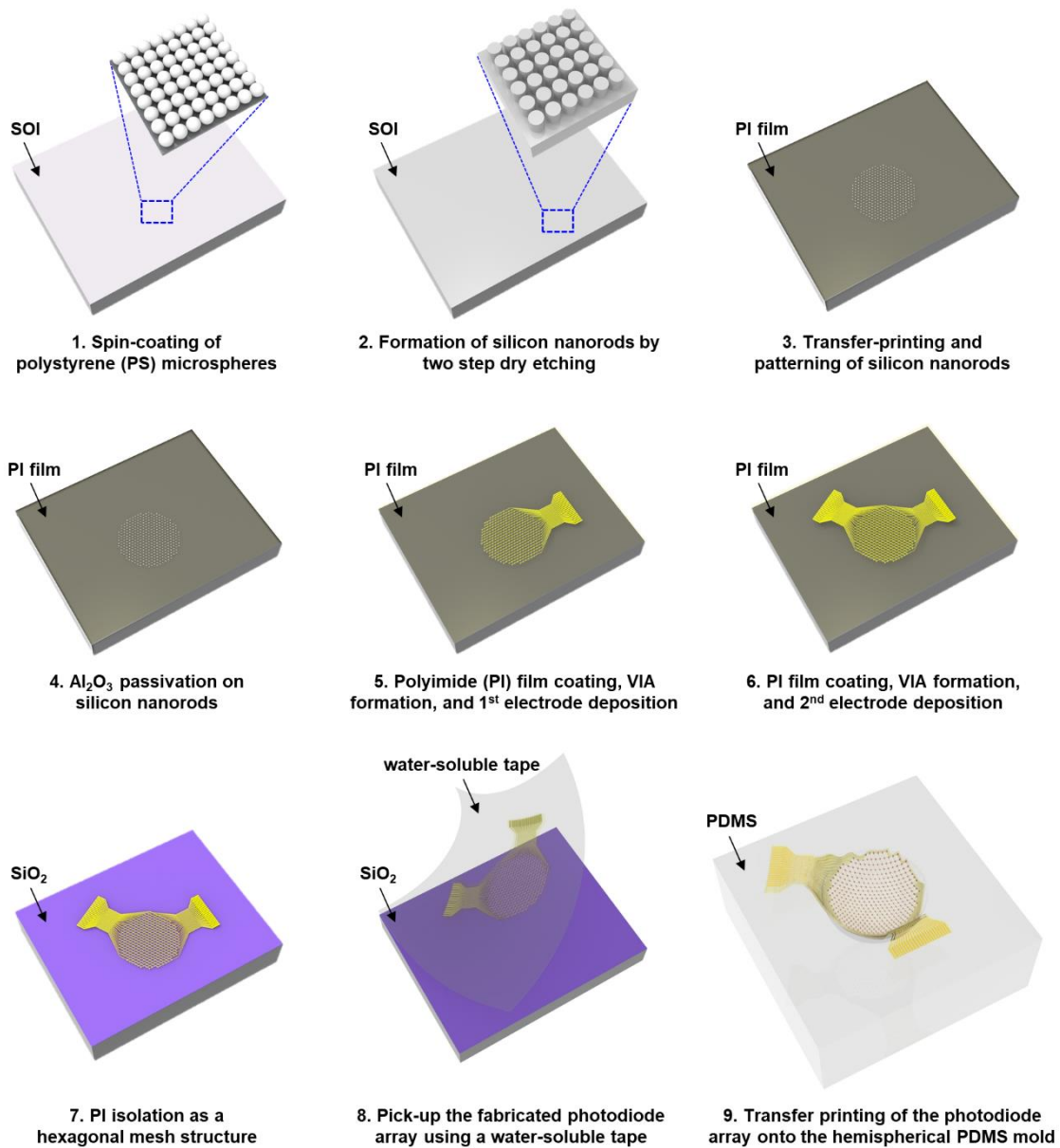


Supplementary Figure 15 | Visual accommodation of the monocentric lens. **a**, Imaging simulation for distant objects located at different d_o . The clear images are obtained for objects located at $d_o = 20 \text{ cm} \sim \text{infinity}$. **b,c**, Imaging simulation for close objects located at various d_o ($d_o < 5 \text{ cm}$). The images focused by the monocentric lens with $d_{i,far}$ are blurred (**b**), but they can be easily accommodated by adjusting d_i for each d_o (**c**). **d**, Schematic illustration showing the visual accommodation for focusing objects located at the distant (left) and close (right) position.

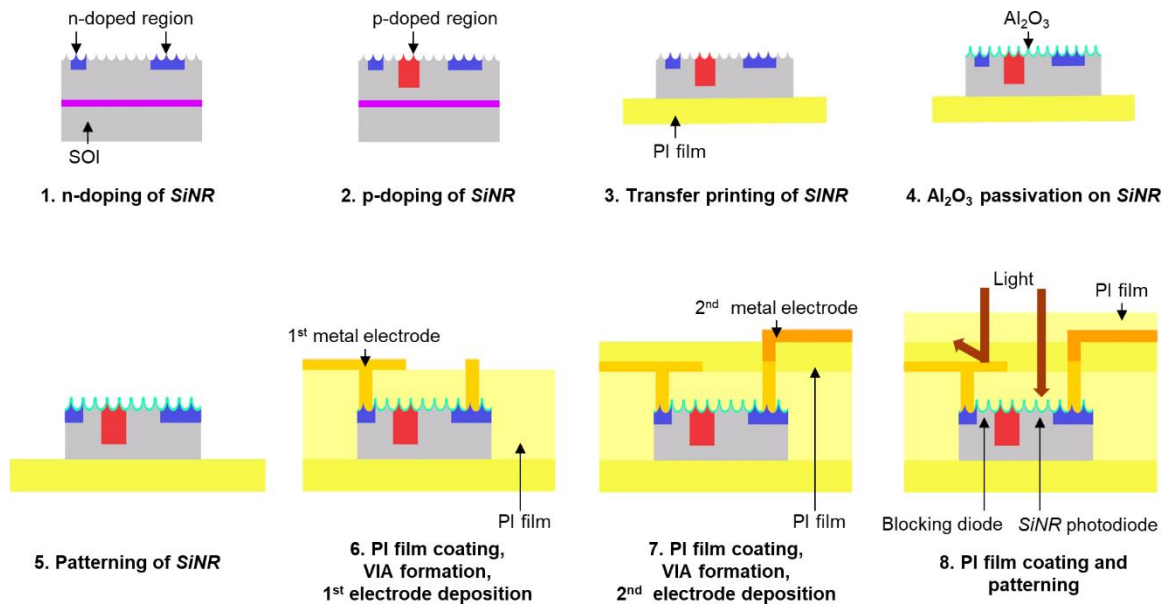


Supplementary Figure 16 | Schematic circuit diagram of the passive matrix array.

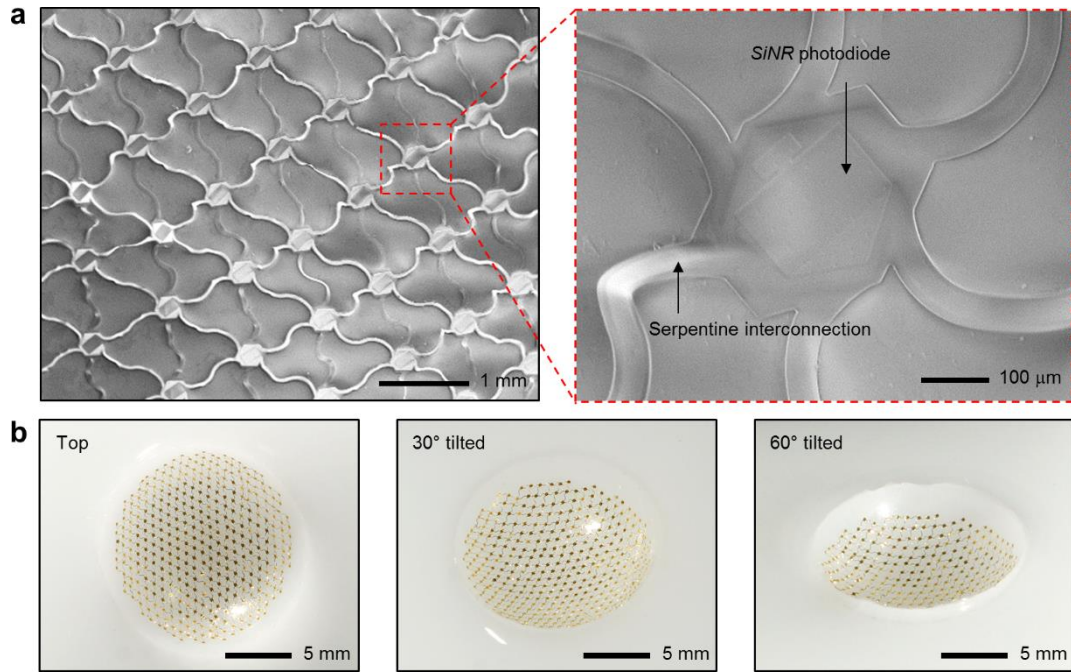
Schematic circuit diagram of the array (top) and a magnified view (bottom) showing the connection of the nanorod-textured silicon photodiode and the blocking diode in a single pixel for the passive matrix array operation. The top inset shows an optical microscope image of the *SiNR* photodiode array.



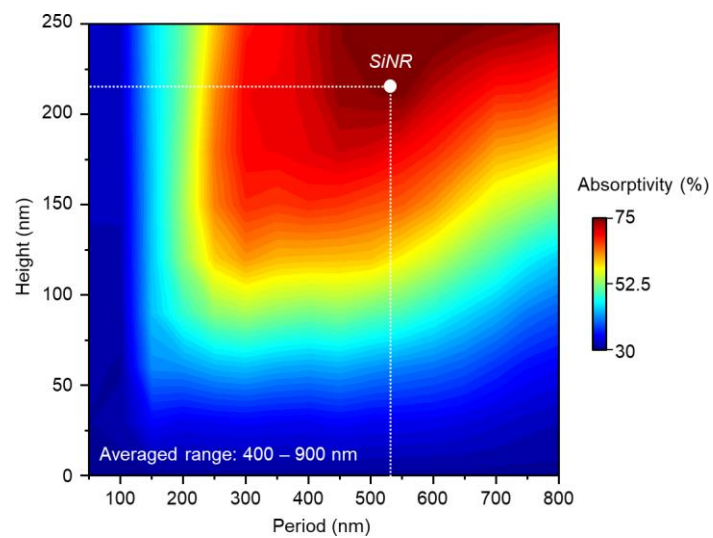
Supplementary Figure 17 | Fabrication process of the hemispherical silicon nanorod photodiode array. Schematic illustrations showing the fabrication process of the *h*-SiNR-PDA.



Supplementary Figure 18 | Fabrication process of the silicon nanorod photodiode and the blocking diode. The cross-sectional schematic illustrations showing the fabrication process of an individual pixel (*i.e.*, the SiNR photodiode with the blocking diode).

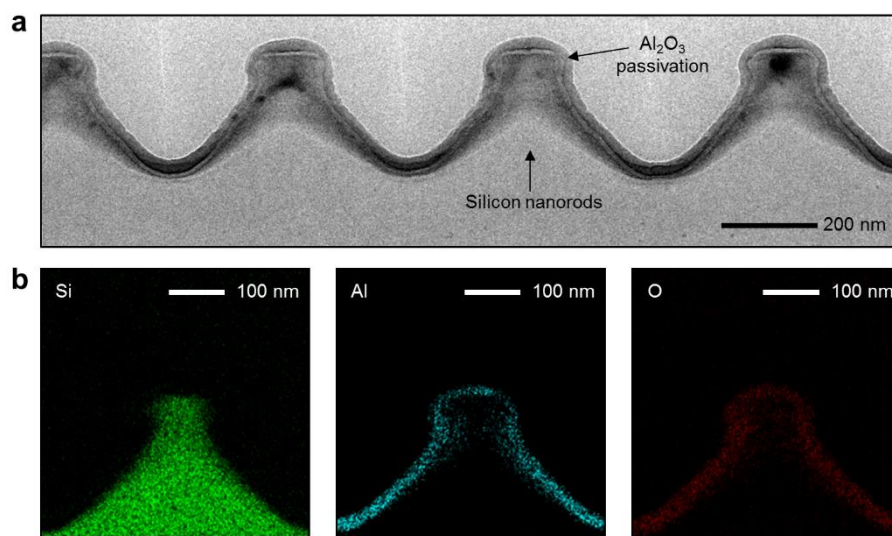


Supplementary Figure 19 | Hemispherical silicon nanorod photodiode array. **a**, Scanning electron microscope image of the center part of the *h*-SiNR-PDA (left) and a magnified view for its individual pixel (right). **b**, Optical camera images of the *h*-SiNR-PDA for the top (left) and tilted (30° and 60° for middle and right) view.

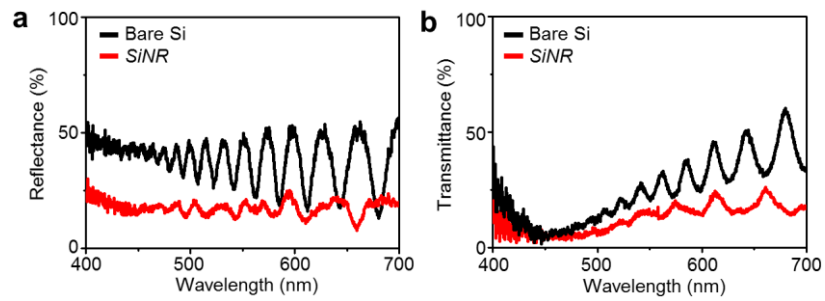


Supplementary Figure 20 | Simulation for the average absorptivity of silicon nanorods.

Contour plot for the average absorptivity of *SiNR* from 400 nm to 900 nm. The total Si thickness is set to be 1.25 μm .

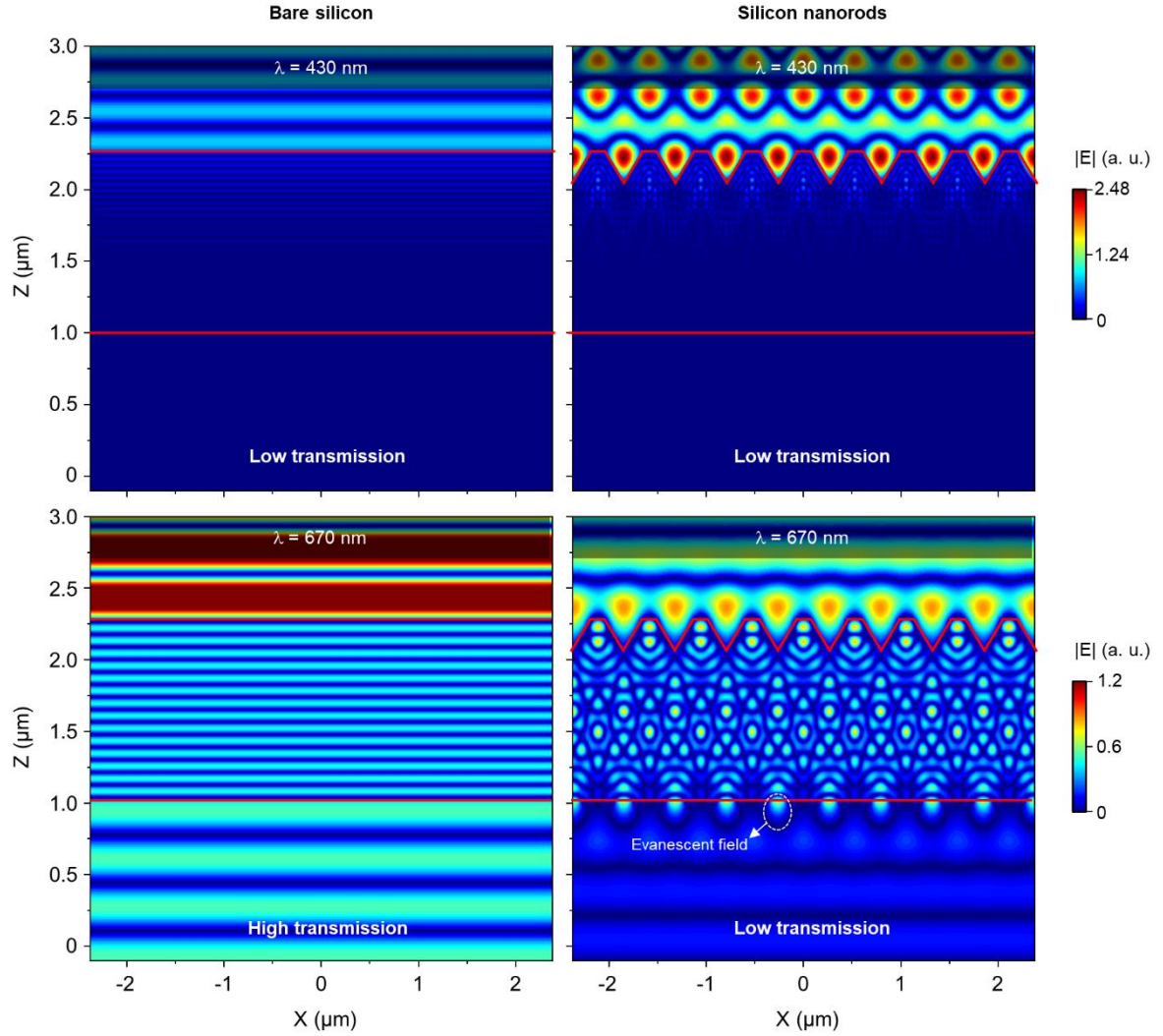


Supplementary Figure 21 | Characterisations of the silicon nanorods and Al_2O_3 passivation layer. **a**, Cross-sectional TEM image of the *SiNR* passivated with a thin Al_2O_3 layer. **b**, EDS scan data of the *SiNR*. The EDS scan analyses show the elemental distribution of Si (green; left), Al (cyan; middle), and O (red; right), and show the shape of the Al_2O_3 layer.

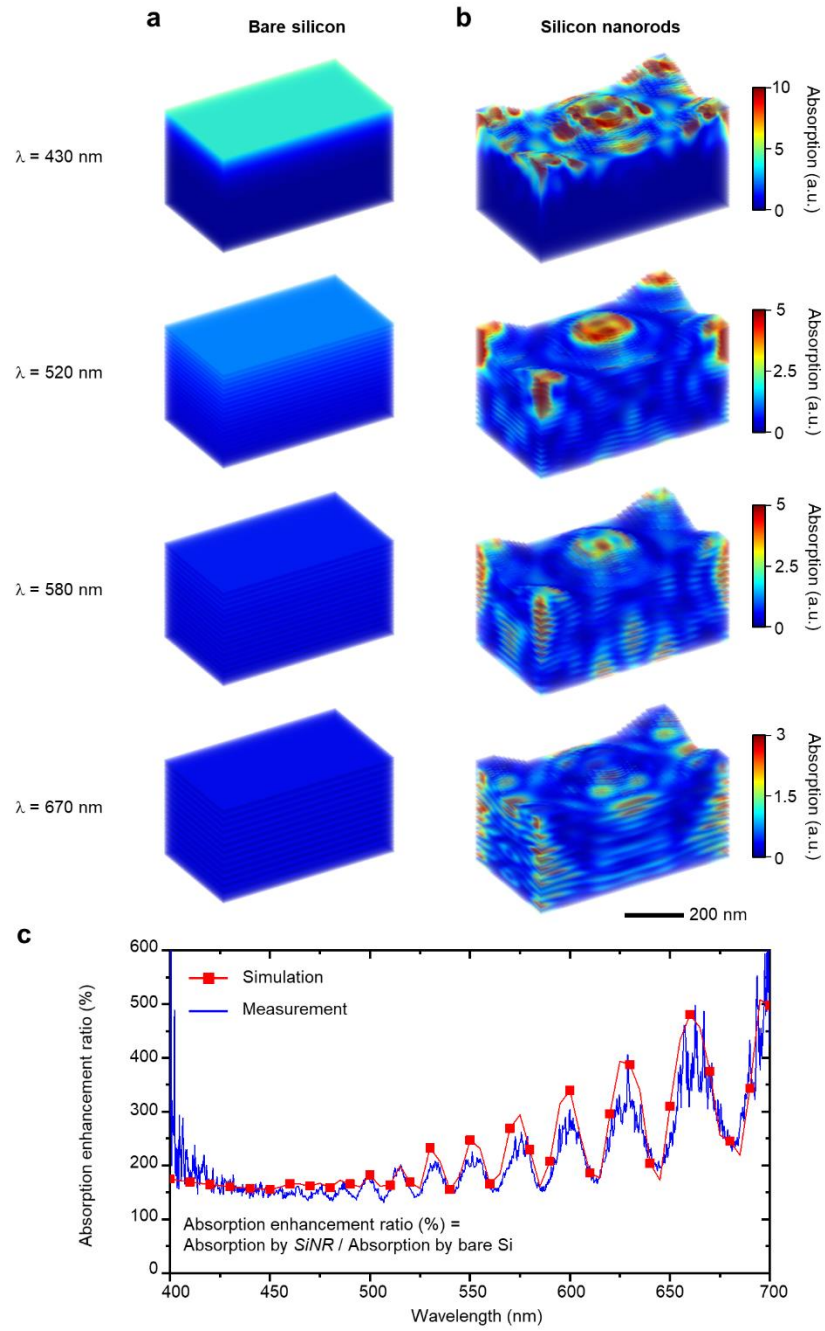


Supplementary Figure 22 | Optical characteristics of bare silicon and silicon nanorods.

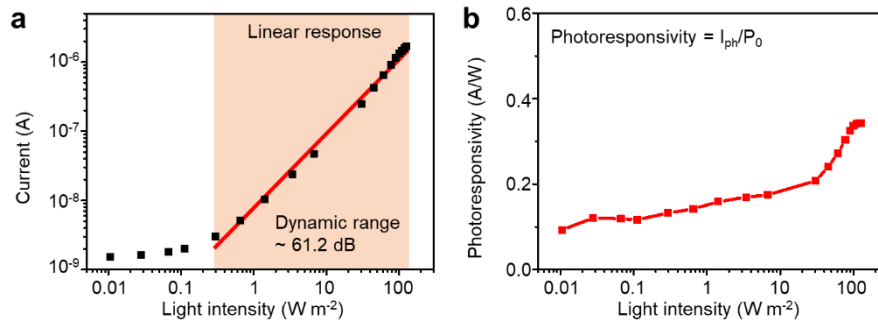
a,b, Reflectance (a) and transmittance (b) of the bare silicon and *SiNR* in the visible spectrum range.



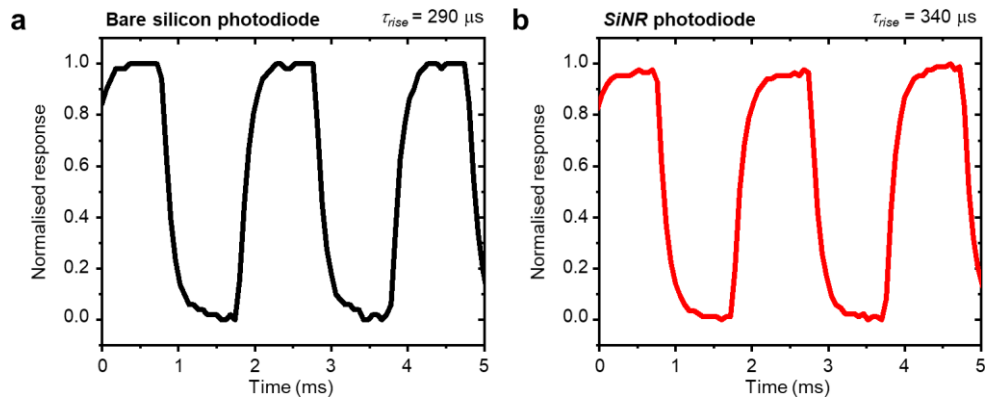
Supplementary Figure 23 | Simulation for short and long wavelength electric field distributions. Contour plots for the electric field distribution of the bare silicon and the *SiNR*. The *SiNR* have the period of 520 nm and height of 220 nm. A plane wave launched at $Z = 3 \mu\text{m}$ with the downward propagating direction was used.



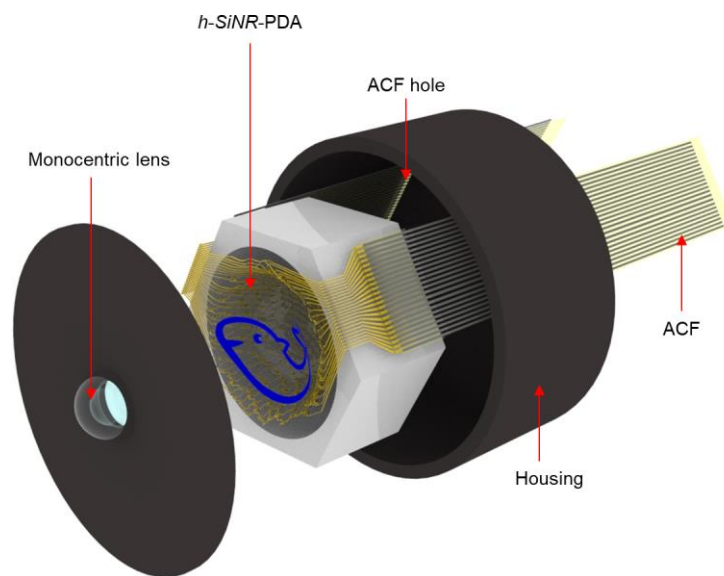
Supplementary Figure 24 | Three-dimensional absorption in the bare silicon and silicon nanorods. a,b, Theoretical optical analyses of the three-dimensional absorption profile in the bare silicon (**a**) and *SiNR* (**b**) with the thickness of $1.25 \mu\text{m}$ under the illumination of the various wavelength lights in the visible spectrum range. **c,** Simulated and measured absorption enhancement ratio of the *SiNR* compared to those of the bare silicon.



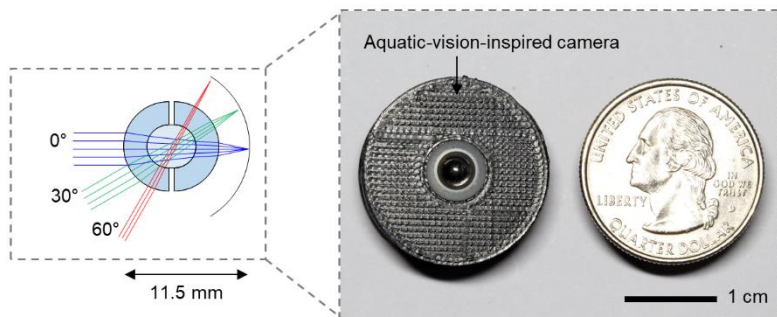
Supplementary Figure 25 | Dynamic range and photoresponsivity. a,b, Characterisation of the dynamic range (**a**) and photoresponsivity (**b**) for the *SiNR* photodiode serially connected with the blocking diode. Its dynamic range is 61.2 dB, and its photoresponsivity is 0.34 A W^{-1} at the light intensity of 100 W m^{-2} . I_{ph} indicates the photocurrent in the *SiNR* photodiode, and P_0 indicates the intensity of the incident light.



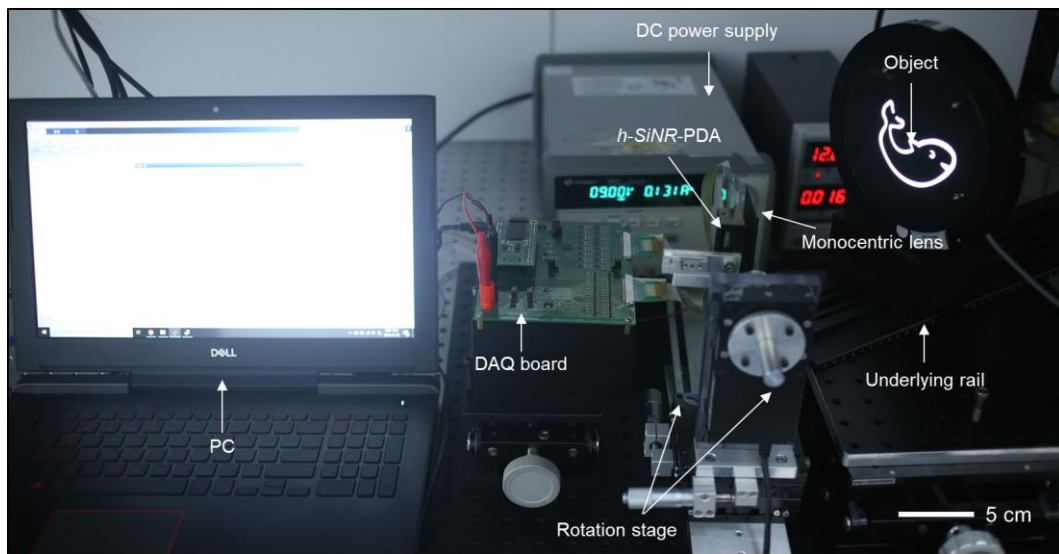
Supplementary Figure 26 | Photoresponse speed. a,b, Temporal photocurrent characteristics of the bare silicon photodiode (**a**) and of the *SiNR* photodiode with Al_2O_3 passivation (**b**). The rise time (τ_{rise}) of the bare silicon photodiode and the *SiNR* photodiode are 290 μ s and 340 μ s, respectively.



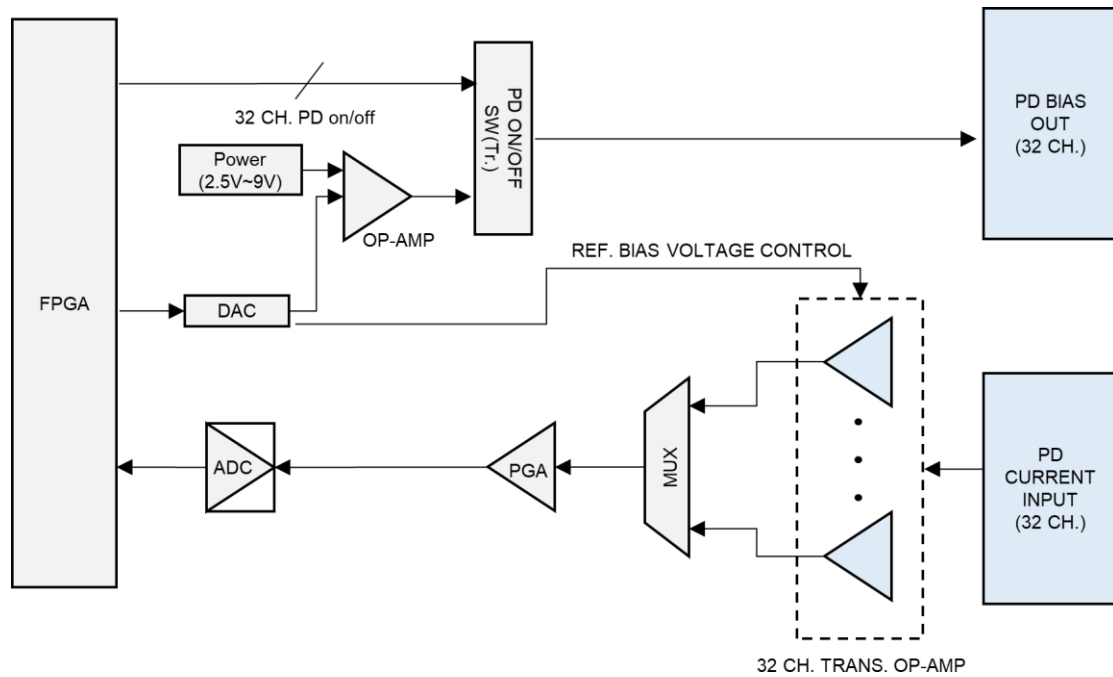
Supplementary Figure 27 | Aquatic-vision-inspired camera module. Exploded schematic illustration of the aquatic-vision-inspired camera module, comprised of a monocentric lens, a *h*-SiNR-PDA, a housing, and the ACF for wiring.



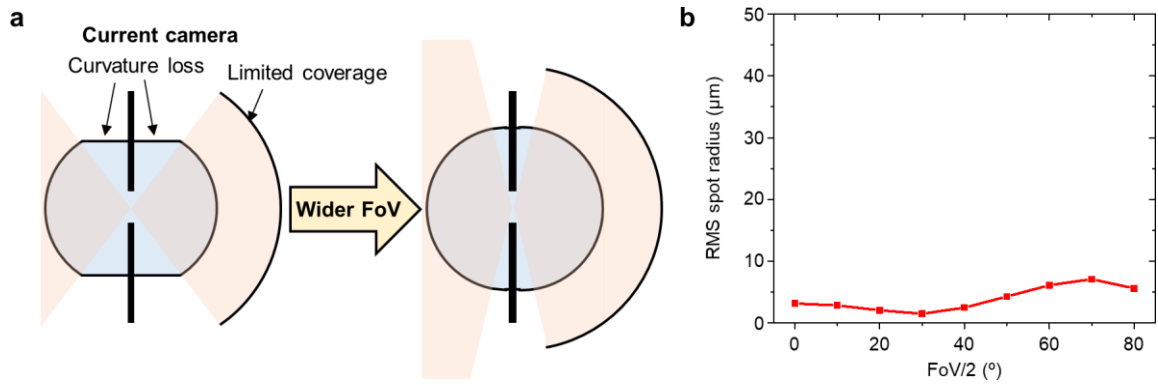
Supplementary Figure 28 | Module size of the aquatic-vision-inspired camera. Ray tracing simulation of the aquatic-vision-inspired camera module (left). The right photograph shows the aquatic-vision-inspired camera module compared to a quarter coin.



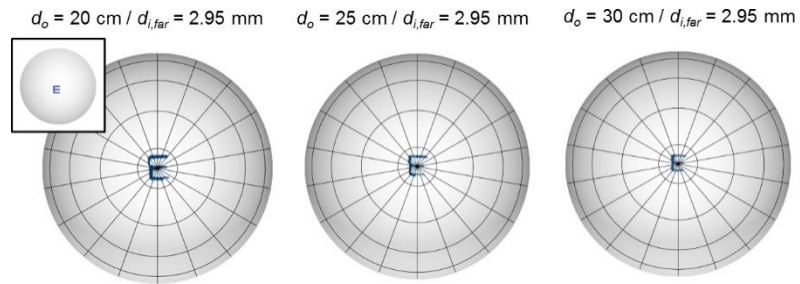
Supplementary Figure 29 | Experimental setup for the imaging demonstration. Optical camera image of the experimental setup including the data acquisition system. The shadow mask mounted on the light source generates the object, whose image is captured by the aquatic-vision-inspired camera. The underlying rails and rotation stages control the distances and angles of the object.



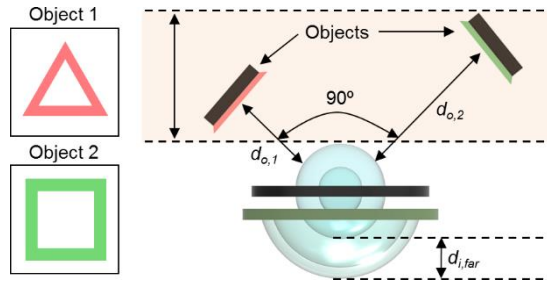
Supplementary Figure 30 | Schematic diagram of the customised FPGA-based data acquisition board. For real-time signal readout, the FPGA handles the 32 by 32 channel data with the 2 GHz clock speed. The digitiser is composed of an analog to digital converter (ADC), a programmable gain-amplifier (PGA), a multiplexer (MUX), a digital to analog converter (DAC), a regulated DC power, and OP-AMPs.



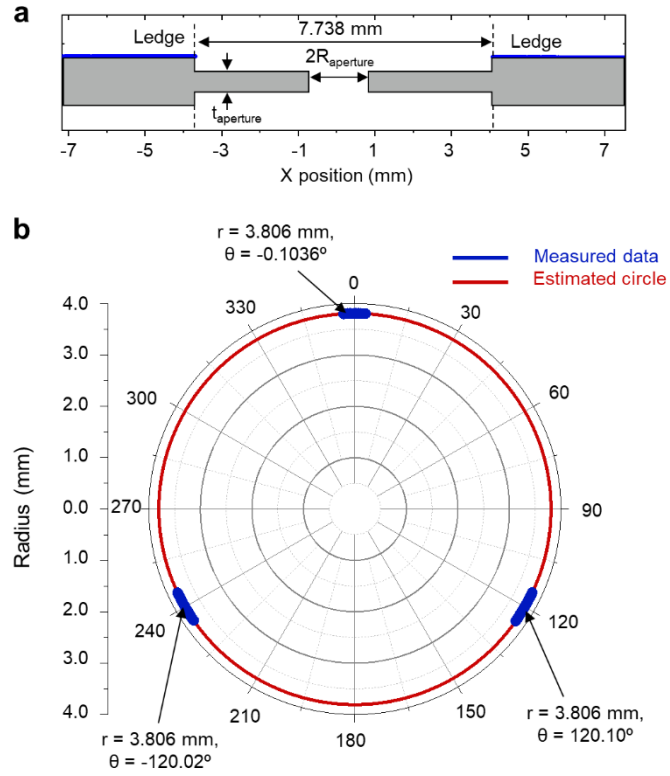
Supplementary Figure 31 | Field-of-view of the aquatic-vision-inspired camera. **a**, The current aquatic-vision-inspired camera with the limited FoV of 120° due to the monocentric lens with a periphery curvature loss and the *h-SiNR*-PDA with the limited coverage (left). The FoV can be improved by applying an injection molding method and by employing an image sensor array with the more hemispherical shape (right). **b**, Optical simulation for the focal spot radius when the monocentric lens with the zero curvature loss and the completely hemispherical image sensor array are used. The focal spot radius is maintained below $10\ \mu\text{m}$ with the FoV of 160° .



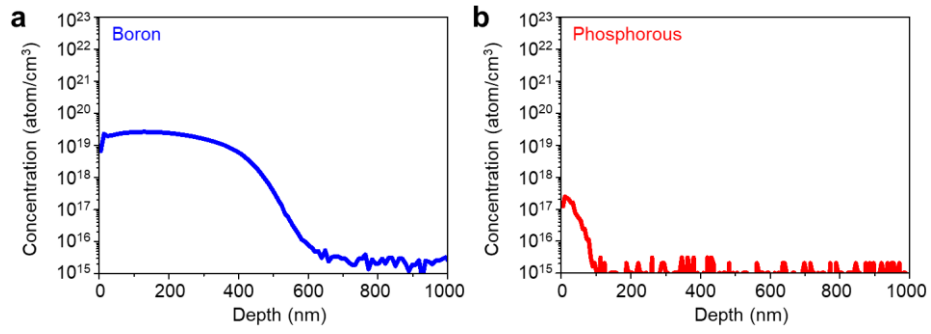
Supplementary Figure 32 | Imaging demonstration that shows the deep depth-of-field characteristics. All the objects, located at 20 cm (left), 25 cm (middle), and 30 cm (right), can be imaged with a single $d_{i, \text{far}} = 2.95 \text{ mm}$. The inset shows the original distant object.



Supplementary Figure 33 | Imaging experiment to demonstrate the deep depth-of-field and wide field-of-view characteristics. Schematic illustration of the experimental setup for the demonstration of both the deep DoF and wide FoV imaging. The left inset shows the original objects (*i.e.*, triangle (object 1) and square (object 2)).



Supplementary Figure 34 | Surface profile of the aperture and the shell lens. a, b, Surface profile of the aperture (**a**) and the shell lens (**b**). The measured size of the ledge is 7.738 mm. The measured aperture diameter (*i.e.*, $2R_{\text{aperture}}$) and thickness (*i.e.*, t_{aperture}) are 1.86 mm and 0.47 mm, respectively. The measured radius of the shell lens is 3.806 mm.



Supplementary Figure 35 | Doping profile in the silicon nanorod photodiode. a,b, Secondary ion mass spectroscopy result of the boron-doped (p-type) region (**a**) and the phosphorous-doped (n-type) region (**b**).

Supplementary Tables

Table 1 Monocentric lens with two RI values (F/# = 2.63)						
Surface	Radius (mm)	Thickness (mm)	Material	RI	Abbe number	Semi-diameter (mm)
OBJECT	Infinity	Infinity	-	-	-	Infinity
1	4.100	2.100	SF16	1.65	34.0	4.100
2	2.000	2.000	BK7	1.52	64.2	2.000
STOP	Infinity	0.500	NOA 61	1.56	42.4	1.000
4	Infinity	2.000	BK7	1.52	64.2	1.700
5	-2.000	2.100	SF16	1.65	34.0	2.000
6	-4.100	2.789	-	-	-	4.100
IMAGE	-7.500	-	-	-	-	7.500

Supplementary Table 1 | Information about the lens components of the monocentric lens with two different RI values. The radii, thicknesses, materials, RI values, Abbe numbers at d-line (*i.e.*, 588 nm), and semi-diameters of the lens components used in the monocentric lens are summarised.

Table 2 Monocentric lens with three RI values (F/# = 2.63)						
Surface	Radius (mm)	Thickness (mm)	Material	RI	Abbe number	Semi-diameter (mm)
OBJECT	Infinity	Infinity	-	-	-	Infinity
1	4.100	1.256	ADC2	1.60	55.3	4.100
2	2.844	1.096	BAFL6	1.59	52.9	3.827
3	1.728	1.728	BK7	1.52	64.2	2.724
STOP	Infinity	0.500	NOA 61	1.56	42.4	1.000
4	Infinity	1.728	BK7	1.52	64.2	3.589
5	-1.728	1.096	BAFL6	1.59	52.9	2.724
6	-2.844	1.256	ADC2	1.60	55.3	3.843
7	-4.100	2.547	-	-	-	5.090
IMAGE	-6.857	-	-	-	-	6.754

Supplementary Table 2 | Information about the lens components of the monocentric lens with three different RI values. The radii, thicknesses, materials, RI values, Abbe numbers at d-line (*i.e.*, 588 nm), and semi-diameters of the lens components used in the monocentric lens with three different RI values are summarised.

	Protruding monocentric lens (Parabolic RI profile, Full aperture)	Protruding monocentric lens (Parabolic RI profile, Small aperture)	Monocentric lens (Two RI values, Small aperture)	Monocentric lens (Three RI values, Small aperture)
Simulated Field-of- view	120°	120°	120°	120°
Spot radius	20.7 ~ 26.9 μm	6.4 ~ 7.5 μm	1.5 ~ 6.1 μm	4.7 ~ 6.1 μm
Ambient environm ent	Water	Water	Air	Air
Refractive index profile	Parabolic (1.377 to 1.540)	Parabolic (1.377 to 1.540)	Two discrete RIs (1.65 (SF16) / 1.52 (BK7))	Three discrete RIs (1.60 (ADC2) / 1.59 (BAFL6) / 1.52 (BK7))
F/#	0.9	2.63	2.63	2.63

Supplementary Table 3 | Comparison of specifications between the monocentric lenses with different RI profiles. The simulated FoV is 120° in all lenses. The natural protruding monocentric lenses have parabolic RI profile from 1.377 to 1.540^{S5}. The monocentric lenses with two different RI values and three different RI values are composed of SF16/BK7 and ADC2/BAFL6/BK7, respectively. These lens materials were optimised through the global optimisation process. The F-numbers were set as 2.63 for fair comparison.

Table 4 Conventional wide angle multi-lens (F/# = 2.63)						
Surface	Radius (mm)	Thickness (mm)	Material	RI	Abbe number	Semi-diameter (mm)
OBJECT	Infinity	Infinity	-	-	-	Infinity
1	-117.300	3.162	N-SK4	1.61	58.6	18.081
2	16.378	1.168	-	-	-	12.724
3	17.551	6.871	SF1	1.72	29.5	12.645
4	-69.066	2.718	N-SK4	1.61	58.6	12.472
5	11.336	5.245	-	-	-	8.327
6	-23.402	1.765	SF1	1.72	29.5	8.304
7	-19.359	2.629	N-SK4	1.61	58.6	8.311
8	-27.730	14.427	-	-	-	8.218
STOP	Infinity	3.797	-	-	-	4.202
10	-84.131	2.870	N-SK4	1.61	58.6	5.966
11	-25.071	0.267	-	-	-	6.654
12	325.992	4.318	N-SK4	1.61	58.6	7.078
13	-13.186	1.854	SF1	1.72	29.5	7.453
14	-53.364	9.627	-	-	-	8.242
15	104.798	2.629	SF1	1.72	29.5	11.229
16	30.725	0.267	-	-	-	11.689
17	31.138	5.613	N-SK4	1.61	58.6	11.899
18	-43.514	0.902	-	-	-	12.119
19	27.558	4.026	N-SK4	1.61	58.6	12.432
20	427.548	20.271	-	-	-	12.240
Image	Infinity	-	-	-	-	7.648

Supplementary Table 4 | Information about the lens components of the conventional wide angle multi-lens. The radii, thicknesses, materials, RI values, Abbe numbers at d-line (*i.e.*, 588 nm), and semi-diameters of the lens components used in the conventional wide angle multi-lens are summarised.

Table 5 Homogeneous ball lens (F/# = 2.63)						
Surface	Radius (mm)	Thickness (mm)	Material	RI	Abbe number	Semi-diameter (mm)
OBJECT	Infinity	Infinity	-	-	-	Infinity
1	4.900	4.900	BK7	1.52	64.2	4.900
STOP	Infinity	0.500	NOA 61	1.56	42.4	1.000
4	Infinity	4.900	BK7	1.52	64.2	1.700
5	-4.900	3.085	-	-	-	4.900
IMAGE	-7.500	-	-	-	-	7.500

Supplementary Table 5 | Information about the lens components of the homogeneous ball lens. The radii, thicknesses, materials, RI values, Abbe numbers at d-line (*i.e.*, 588 nm), and semi-diameters of the lens components used in the homogeneous ball lens are summarised.

Table 6 Image sensor specification								
Image sensor	<i>Andor Zyla4.2 Plus</i>	<i>Photonfocus Sony IMX174</i>	<i>Allied Vision Sony ICX445</i>	<i>Artificial human eye</i>	<i>Artificial fly eye</i>	<i>Hemispherical electronic eye</i>	<i>Smart contact lens</i>	<i>Aquatic-vision-inspired camera</i>
Sensor type	sCMOS	CMOS	CCD	PDA	PDA	PDA	PDA	PDA
Pixel size	6.5×6.5 μm^2	5.86×5.86 μm^2	3.75×3.75 μm^2	500×500 μm^2	270×190 μm^2	113×113×2 $\sqrt{3}$ μm^2 (hexagon)	200×200 μm^2	200×125 μm^2
Number of pixels	2048×2048	1936×1216	1348×976	256	180	676	64	351
Dark current	0.0003 nA/cm ²	0.0476 nA/cm ²	0.1092 nA/cm ²	0.5~2 nA/pixel	N.A.	0.4 nA/pixel	3.95 nA/pixel	0.6 nA/pixel
Dynamic range	33,000:1	3,980:1	822:1	200~800:1	N.A.	1950:1	258:1	>1,000:1
QE	82%	45%	56%	N.A.	N.A.	2.2%	N.A.	58.5%
Sensor shape	Flat	Flat	Flat	Curved	Hemispherical	Hemispherical	Curved	Hemispherical
Radius of curvature	Infinity	Infinity	Infinity	~ 10 mm	~ 7 mm	~ 2.27 mm	N.A.	7.5 mm
Optical system	Multi-lens (Relay lens)	Multi-lens (Relay lens)	Multi-lens (Relay lens)	Single lens (Plano-convex)	Multi-lens (Microlens array)	Single lens (Plano-convex)	N.A.	Single lens (Monocentric lens)
Reference	S12	S13	S14	S8	S11	S15	S16	-

Supplementary Table 6 | Specifications of the image sensors. Comparison of the state-of-the-art image sensors (red) and bio-inspired image sensors (blue) in terms of a sensor type, a pixel size, the dark current, a dynamic range, a quantum efficiency (QE), a sensor shape, the radius of curvature, and the optical system. The commercial ones show the exceptional spatial resolution and sensitivity due to the small pixel size and low dark current. However, the bio-inspired image sensors can simplify the optical system configuration. Among the bio-inspired image sensors, the aquatic-vision-inspired camera demonstrates the low dark current, the high QE, and the hemispherical shape of the image sensor array.

Supplementary References

- S1. Ogura, T. Wide-angle lens system with corrected lateral aberration. U.S. Patent 3589798 (Mar. 25, 1968).
- S2. Shimizu, Y. Fisheye lens systems. U.S. Patent 3734600 (Dec. 16, 1971).
- S3. Horimoto, M. Fish eye lens system. U.S. Patent 4412726 (Jan. 13, 1981).
- S4. Nakagawa, J. Ultra-wide angle photographic lens. U.S. Patent 3741630A (Nov. 5, 1971).
- S5. Jagger, W. S. & Sands, P. J. A wide-angle gradient index optical model of the crystalline lens and eye of the rainbow trout. *Vision Res.* **36**, 2623-2639 (1996).
- S6. <https://www.norlandprod.com/literature/61tds.pdf>
- S7. Steel, W. H. On the choice of glasses for cemented achromatic aplanatic doublets. *Aust. J. Phys.* **7**, 244-253 (1954).
- S8. Ko, H. C. *et al.* A hemispherical electronic eye camera based on compressible silicon optoelectronics. *Nature* **454**, 748–753 (2008).
- S9. Choi, C. *et al.* Human eye-inspired soft optoelectronic device using high-density MoS₂-graphene curved image sensor array. *Nat. Commun.* **8**, 1664 (2017).
- S10. Artal, P. Optics of the eye and its impact in vision: a tutorial. *Adv. Opt. Photon.* **6**, 340–367 (2014).
- S11. Song, Y. M. *et al.* Digital cameras with designs inspired by the arthropod eye. *Nature* **497**, 95–99 (2013).
- S12. <https://andor.oxinst.com/products/scmos-camera-series/zyla-4-2-scmos>
- S13. <https://en.ids-imaging.com/sony-imx174.html>
- S14. <https://s1-dl.theimagingsource.com/api/2.5/packages/publications/sensors->

ccd/icx445aqa/d126cbfa-e767-5034-a3a4-1ee0dabf9f63/icx445aqa_1.2.en_US.pdf

S15. Zhang, K., *et al.* Origami silicon optoelectronics for hemispherical electronic eye systems.

Nat. Commun. **8**, 1782 (2017).

S16. Sim, K., *et al.* Three-dimensional curvy electronics created using conformal additive stamp printing. *Nat. Electron.* **2**, 471-479 (2019).